

The AGORA High-resolution Galaxy Simulations Comparison Project. X: Formation and Evolution of Galaxies at the High-redshift Frontier

HYEONYONG KIM ^{1,*} JI-HOON KIM ^{2,3,4} MINYONG JUNG ⁵ SANTI ROCA-FÀBREGA ^{6,7,*} DANIEL CEVERINO ^{8,9}
PABLO GRANIZO ^{8,10,*} KENTARO NAGAMINE ^{10,11,12,13,14} JOEL R. PRIMACK ¹⁵ HÉCTOR VELÁZQUEZ ^{16,*}
KIRK S. S. BARROW ¹⁷ ROBERT FELDMANN ¹⁸ KEITA FUKUSHIMA ³ LUCIO MAYER ¹⁹ BOON KIAT OH ^{20,21}
JOHNNY W. POWELL ²² TOM ABEL ^{23,24,25} CHAERIN JEONG ²⁶ ALESSANDRO LUPI ^{27,28} YURI OKU ²⁹
THOMAS R. QUINN ³⁰ YVES REVAZ ³¹ RAMÓN RODRÍGUEZ-CARDOSO ^{32,33,34} IKKOH SHIMIZU ³⁵ ROMAIN TEYSSIER ³⁶
AND AGORA COLLABORATION³⁷

¹Center for Theoretical Physics, Department of Physics and Astronomy, Seoul National University, Seoul 08826, Republic of Korea; gusdyd398@snu.ac.kr

²Center for Theoretical Physics, Department of Physics and Astronomy, Seoul National University, Seoul 08826, Republic of Korea; mornkr@snu.ac.kr

³Institute for Data Innovation in Science, Seoul National University, Seoul 08826, Republic of Korea

⁴Seoul National University Astronomy Research Center, Seoul 08826, Republic of Korea

⁵Center for Theoretical Physics, Department of Physics and Astronomy, Seoul National University, Seoul 08826, Republic of Korea; wispedia@snu.ac.kr

⁶Lund Observatory, Division of Astrophysics, Department of Physics, Lund University, SE-221 00 Lund, Sweden; santi.roca.fabrega@fysik.lu.se

⁷Departamento de Física de la Tierra y Astrofísica, Facultad de Ciencias Físicas, Plaza Ciencias, 1, 28040 Madrid, Spain

⁸Universidad Autónoma de Madrid, Ciudad Universitaria de Cantoblanco, E-28049 Madrid, Spain

⁹CIAFF, Facultad de Ciencias, Universidad Autónoma de Madrid, E-28049 Madrid, Spain

¹⁰Theoretical Astrophysics, Department of Earth and Space Science, Graduate School of Science, Osaka University, Toyonaka, Osaka, 560-0043, Japan

¹¹Theoretical Joint Research, Forefront Research Center, Graduate School of Science, Osaka University, Toyonaka, Osaka 560-0043, Japan

¹²Kavli IPMU (WPI), University of Tokyo, 5-1-5 Kashiwanoha, Kashiwa, Chiba, 277-8583, Japan

¹³Department of Physics & Astronomy, University of Nevada Las Vegas, Las Vegas, NV 89154, USA

¹⁴Nevada Center for Astrophysics, University of Nevada, Las Vegas, 4505 S. Maryland Pkwy, Las Vegas, NV 89154-4002, USA

¹⁵Department of Physics, University of California at Santa Cruz, Santa Cruz, CA 95064, USA

¹⁶Instituto de Astronomía, Universidad Nacional Autónoma de México, A.P. 70-264, 04510, Mexico, D.F., Mexico

¹⁷Department of Astronomy, University of Illinois at Urbana-Champaign, Urbana, IL 61801, USA

¹⁸Department of Astrophysics, University of Zurich, Zurich CH-8057, Switzerland

¹⁹Department of Astrophysics, University of Zurich, Winterthurerstrasse 190, CH-8057 Zürich, Switzerland

²⁰Department of Physics, University of Connecticut, U-3046, Storrs, CT 06269, USA

²¹School of Physics, Korea Institute for Advanced Study, 85 Hoegiro, Dongdaemun-gu, Seoul 02455, Republic of Korea

²²Department of Physics, Reed College, Portland, OR 97202, USA

²³Kavli Institute for Particle Astrophysics and Cosmology, Stanford University, Stanford, CA 94305, USA

²⁴Department of Physics, Stanford University, Stanford, CA 94305, USA

²⁵SLAC National Accelerator Laboratory, Menlo Park, CA 94025, USA

²⁶Department of Astronomy & Space Science, Kyung Hee University, 1732 Deogyong-daero, Yongin-si, Gyeonggi-do 17104, Republic of Korea

²⁷Como Lake Center for Astrophysics, DiSAT, Università degli Studi dell'Insubria, via Valleggio 11, 22100, Como, Italy

²⁸INAF, Osservatorio Astronomico di Bologna, Via Gobetti 93/3, I-40129 Bologna, Italy

²⁹Center for Cosmology and Computational Astrophysics, Institute for Advanced Study in Physics, Zhejiang University, Hangzhou 310027, People's Republic of China

³⁰Department of Astronomy, University of Washington, Seattle, WA 98195, USA

³¹Institute of Physics, Laboratoire d'Astrophysique, École Polytechnique Fédérale de Lausanne (EPFL), CH-1015 Lausanne, Switzerland

³²Departamento de Física de la Tierra y Astrofísica, Fac. de C.C. Físicas, Universidad Complutense de Madrid, E-28040 Madrid, Spain

³³GMV, Space and Avionics Equipment, Isaac Newton, 11 Tres Cantos, E-28760 Madrid, Spain

³⁴Instituto de Física de Partículas y del Cosmos, IPARCOS, Fac. C.C. Físicas, Universidad Complutense de Madrid, E-28040 Madrid, Spain

³⁵Shikoku Gakuin University, 3-2-1 Bunkyocho, Zentsuji, Kagawa, 765-8505, Japan

³⁶Department of Astrophysical Sciences, Princeton University, 4 Ivy Lane, Princeton, NJ 08540, USA

³⁷<http://www.AGORAsimulations.org>

ABSTRACT

Recent observations from JWST have revealed unexpectedly luminous galaxies, exhibiting stellar masses and luminosities significantly higher than predicted by theoretical models at Cosmic Dawn. In this study, we present a suite of cosmological zoom-in simulations targeting high-redshift ($z \geq 10$) galaxies with dark matter halo masses in the range $10^{10} - 10^{11} M_{\odot}$ at $z = 10$, using state-of-the-art galaxy formation simulation codes (ENZO, RAMSES, CHANGA, GADGET-3, GADGET-4, and GIZMO). This study aims to evaluate the convergence of the participating codes and their reproducibility of high-redshift galaxies with the galaxy formation model calibrated at relatively low redshift, without additional physics for high-redshift environments. The sub-grid physics follows the *AGORA CosmoRun* framework, with adjustments to resolution and initial conditions to emulate similar physical environments in the early universe. The participating codes show consistent results for key galaxy properties (e.g., stellar mass), but also reveal notable differences (e.g., metallicity), indicating that galaxy properties at high redshifts are highly sensitive to the feedback implementation of the simulation. Massive halos ($M_{\text{halo}} \geq 5 \times 10^{10} M_{\odot}$ at $z = 10$) succeed in reproducing observed stellar masses, metallicities, and UV luminosities at $10 \leq z \leq 12$ without requiring additional subgrid physics, but tend to underpredict those properties at higher redshift. We also find that varying the dust-to-metal ratio modestly affects UV luminosity of simulated galaxies, whereas the absence of dust significantly enhances it. In future work, higher-resolution simulations will be conducted to better understand the formation and evolution of galaxies at Cosmic Dawn.

Keywords: galaxies: high-redshift — galaxies: formation — galaxies: evolution — method: numerical — hydrodynamics

1. INTRODUCTION

Emerging with the first data from the James Webb Space Telescope (JWST), the Cosmic Dawn was unveiled, shedding light on the faintest galaxies ever observed. Although high-redshift objects around $z = 8 - 10$ were detected by the Hubble Space Telescope (HST) (e.g., Ellis et al. 2013; Oesch et al. 2016; Mainali et al. 2018; Finkelstein et al. 2022), galaxies beyond this redshift were too faint to be observed for HST. Since the launch of the JWST, however, numerous studies using the JWST NIRCam data have reported high-redshift galaxy candidates beyond $z = 10$ (e.g., Castellano et al. 2022; Adams et al. 2023; Leung et al. 2023; Finkelstein et al. 2024; Carniani et al. 2024; Robertson et al. 2024; Whitler et al. 2025; Pérez-González et al. 2025).

Although one of the ultra-high-redshift galaxy candidates suggested in early JWST studies (e.g., Donnan et al. 2023; Bouwens et al. 2023; Finkelstein et al. 2023) turned out to be a low-redshift interloper (Arrabal Haro et al. 2023; Harikane et al. 2024), many other candidates have been confirmed through spectroscopic analyses (e.g., Bunker et al. 2023; Tacchella et al. 2023; Wang et al. 2023; Schouws et al. 2025; Harikane et al. 2024, 2025). Observational efforts to detect even more distant galaxies continue to progress rapidly. Recent spectroscopic measurements have confirmed galaxies at redshifts of up to $z = 14$ (e.g., Carniani et al. 2024; Robertson et al. 2024; Whitler et al. 2025) and photometric surveys

have identified galaxy candidates extending to $z = 15 - 25$ (e.g., Pérez-González et al. 2025; Castellano et al. 2025).

JWST observations have also revealed that these high- z galaxies exhibit exceptionally high UV luminosities, creating a strong tension in standard galaxy formation theories within the Λ CDM cosmological framework. Initially, Labbé et al. (2023) reported six massive galaxy candidates with stellar masses greater than $10^{10} M_{\odot}$ at $z = 7.4 - 9.1$. These candidates were several orders of magnitude brighter and more massive than the Λ CDM cosmology prediction, implying baryon-to-stellar conversion ratios approaching unity (Lovell et al. 2023; Boylan-Kolchin 2023). This strong tension was partially resolved after the revision of the paper (Boylan-Kolchin 2023) with calibration of the NIRCam and updated stellar masses. Still, the early universe unveiled by JWST seems to have more luminous galaxies than expected by Λ CDM cosmology.

To alleviate this tension, various explanations have been proposed. Some studies suggest a top-heavy initial mass function (IMF) characterized by a larger fraction of massive stars can enhance the UV luminosity of high- z galaxies (e.g., Inayoshi et al. 2022; Finkelstein et al. 2023; Yung et al. 2024). This fraction could be achieved by the environments of the early universe — low metallicity and high cosmic microwave background (CMB) temperature, which can suppress fragmentation and facilitate the collapse of giant molecular clouds (Chon et al. 2022). Active galactic nuclei (AGN) are also considered as a possible source of UV photons. Several studies, however, suggest that AGNs are not dominant contributors to UV luminosity (e.g., Ono et al.

* Code leaders

2023; Trinca et al. 2024), and their contribution to UV luminosity is still in debate.

Alternatively, Dekel et al. (2023) and Li et al. (2024) propose the feedback-free starburst (FFB) model. According to this model, the free-fall time of dense gas clouds can be shorter than the timescale for stellar wind or supernova feedback effects. Although this condition holds in dense gas environments in very massive halos, this scenario leads to significantly increased star formation efficiencies in early galaxies. Indeed, the FirstLight simulations (Ceverino et al. 2024) have shown that the galaxy-averaged star formation efficiency (SFE) increases at these high redshifts due to higher ISM densities. The so-called attenuation-free model (AFM) has also been proposed to reconcile the tension (e.g., Tsuna et al. 2023; Ferrara et al. 2025). In this model, the radiation outflows from bursty star formation push dust outward, resulting in significantly reduced attenuation, which could also enhance the overabundance of bright galaxies at high redshift.

While a variety of theoretical models to explain high-redshift galaxies are actively proposed and debated, recent numerical simulations suggest the tension may be less severe than initially thought. For example, McCaffrey et al. (2023) argues that the most massive galaxies in Renaissance simulations are consistent with the JWST survey data in stellar mass and star formation rate (SFR). Also, results from the FIRE-2 and FIREbox^{HR} simulations (e.g., Sun et al. 2023; Feldmann et al. 2025) demonstrate that the observed abundance of UV-bright galaxies and the evolution of the UV luminosity density can naturally be explained by the standard galaxy formation model without any additional subgrid physics.

In this paper, we introduce the *AGORA High-z Run*, a suite of zoom-in simulations during Cosmic Dawn based on the *AGORA CosmoRun* model. The *AGORA* simulation comparison project began with the objective of enhancing the reliability and predictive power of numerical galaxy formation simulations (Kim et al. 2014, 2016, hereafter Papers I and II). By comparing multiple state-of-the-art simulations from identical initial conditions and common subgrid physics, the project aims to establish robust and reliable astrophysical models independent of specific simulation codes. Starting from Papers III and IV (Roca-Fàbrega et al. 2021, 2024), the *AGORA* project initiated the *CosmoRun* series. *CosmoRun* is a suite of simulations modeling the formation and evolution of Milky Way-size galaxies (halo mass of $10^{12}M_{\odot}$ at $z=0$) across multiple numerical codes. This series comprehensively examined properties of Milky Way-mass galaxy, satellite galaxy populations, circumgalactic medium (CGM) characteristics, satellite quenching mechanisms, and disk formation of Milky Way-mass galaxy across multiple numerical platforms (Jung et al. 2024; Strawn et al. 2024; Rodríguez-Cardoso et al. 2025; Jung et al. 2025, hereafter Papers V-

Halo	Halo mass ($10^9 M_{\odot}$)					
	$z=10$	$z=11$	$z=12$	$z=13$	$z=14$	$z=15$
HALO 1	15.1	8.89	5.79	3.32	1.83	0.82
HALO 2	15.3	7.76	5.03	3.31	1.71	0.87
HALO 3	46.8	28.6	5.02	3.05	2.09	1.06
HALO 4	51.6	33.4	18.6	8.78	4.88	1.79
HALO 5	81.2	47.7	25.3	15.9	5.96	1.78

Table 1. The mass history of halos selected as the initial conditions. The values are the mean halo mass of six numerical codes.

VIII). The *CosmoRun* simulation has not only demonstrated good agreement with observations in key galaxy properties such as stellar mass and the mass–metallicity relation (MZR), but also revealed similarities and differences in different gravity and hydrodynamics schemes. Now, the *AGORA High-z Run* suite extends the *AGORA* framework to the early universe, focusing on zoom-in simulations of overdense regions that host the earliest, most massive galaxies. By applying the galaxy formation model calibrated in *CosmoRun* to these environments, the *High-z Run* allows us to assess its ability to reproduce luminous high-redshift galaxies observed by JWST, while offering new insights into inter-code agreements and differences at Cosmic Dawn.

This paper is structured as follows. Section 2 provides an overview of the *CosmoRun* and details of the *High-z Run*, including initial conditions, refinement strategies, analysis and mock observation methodologies, and a brief description of participating simulation codes. In Section 3, we analyze the properties and evolution of high- z galaxies from $z=15$ to $z=10$, focusing on gas properties, stellar mass, and metallicity of target halos, and compare these results with JWST spectroscopy data. We also present mock observations of the *High-z Run* and examine the UV brightness of simulated galaxies. Section 4 discusses the star formation rate, efficiency and the role of dust attenuation in the *High-z Run*. Finally, we summarize our findings and provide conclusions in Section 5.

2. SIMULATION

2.1. The *AGORA “High-z Run” Simulation Suite*

The *High-z Run* adopts the subgrid physics framework developed for the *AGORA CosmoRun* simulations (Papers III and IV), which model the formation and evolution of Milky Way-mass galaxy’s halo ($\sim 10^{12}M_{\odot}$ at $z=0$) across multiple numerical codes. The suite involves various numerical methods, including adaptive mesh refinement (AMR), smoothed particle hydrodynamics (SPH), and hybrid techniques. Participating AMR codes include ENZO (Bryan et al. 2014) and RAMSES (Teyssier 2002). SPH codes are represented by CHANGA (Menon et al. 2015), GADGET-3 (Springel

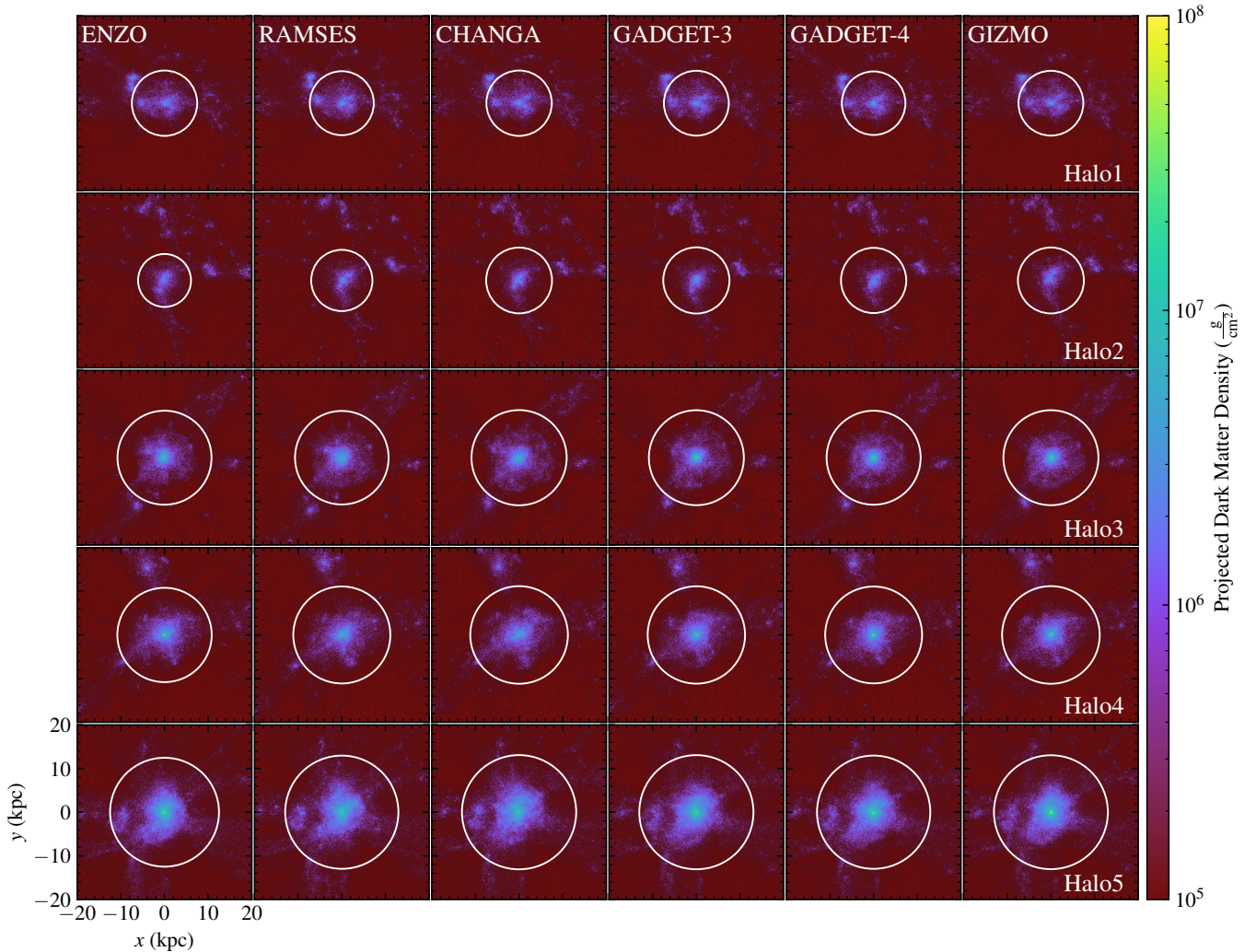


Figure 1. The dark matter surface densities at $z = 10$ for five massive halos across six different hydrodynamical simulations, “*High-z Run*”. The projections are taken through a 40 kpc slice and the target halo’s virial radius R_{vir} identified by the ROCKSTAR halo finder (Behroozi et al. 2013) is denoted with a white circle. The simulations are conducted by Santi Roca-Fàbrega (RAMSES), Hyeonyong Kim (ENZO, GADGET-3, GIZMO), Héctor Velázquez (CHANGA), and Pablo Cuadrado (GADGET-4). See Section 2 for detailed information including subgrid physics, initial condition, and refinement schemes of these simulations.

2005), GADGET-4 (Springel et al. 2021) and GEAR (Revaz & Jablonka 2012). AREPO (Springel 2010) and GIZMO (Hopkins 2015) are classified as hybrid methods. We will refer to AMR codes as mesh-based codes and SPH and hybrid methods as particle-based codes for convenience.

While the gravity and hydrodynamics solvers differ across the participating codes, all simulations employ the GRACKLE chemistry and cooling library (Smith et al. 2017). Based on the gas metallicity, cooling and heating rates are computed from the chemistry tables generated with the photoionization code CLOUDY (Ferland et al. 2013) and a redshift-dependent cosmic UV background (Haardt & Madau 2012) is applied starting at $z = 15$. Star formation occurs when the gas density exceeds the number density $n_{\text{H}} = 1\text{cm}^{-3}$. The local star

formation rate follows the Schmidt law, $\rho_*/dt = \epsilon_*\rho_{\text{gas}}/t_{\text{ff}}$, where $\epsilon_* = 0.01$ is the formation efficiency and local free fall time, $t_{\text{ff}} = (3\pi/32G\rho_{\text{gas}})^{1/2}$. A metallicity floor of $10^{-4} Z_{\odot}$ ¹ is applied to consider the metal enrichment by first stars that cannot be resolved. At the same time, each code follows its own implementation of stellar feedback, feedback energy, and metal diffusion scheme, reflecting the most widely used practice in the community. For more detailed information about the feedback description, we refer readers to Section 3.1 of Paper III and Section 4 of Paper IV.

¹ $Z_{\odot} = 0.02041$ is used across all participating codes, following Paper II (see Section 2 of Paper II for details).

2.2. Initial Conditions and Refinement Scheme

We use MUSIC, a multi-scale initial condition generator code (Hahn & Abel 2011), to generate the initial conditions for the *High-z Run*. We adopt cosmological parameters WMAP7/9+SNe+BAO: $\Omega_\Lambda = 0.728$, $\Omega_{\text{matter}} = 0.272$, $\Omega_{\text{DM}} = 0.227$, $\sigma_8 = 0.807$, $n_s = 0.961$, and $h = 0.702$. Since this paper does not study the population of high-redshift galaxies, we utilize the cosmological parameters from *CosmoRun* for consistency, but plan to use updated cosmological parameters in future high-redshift simulation work. Starting from $z = 100$, we select five halos with $M_{\text{halo}} > 10^{10} M_\odot$ at $z = 10$, representative of observed high-redshift galaxies. Table 1 summarizes the average halo masses at selected epochs. Based on a 256^3 (512^3 for Halo 5) root resolution in a 64 comoving $(\text{Mpc}/h)^3$ box, we set an additional 4 (3 for Halo 5) levels to generate a zoom-in region of a 4096^3 effective resolution. The most refined regions are set to enclose all the particles within $4R_{\text{vir}}$ of the target halos at $z = 10$, and the masses of particles residing in the most refined region are $m_{\text{DM}} = 3.41 \times 10^5 M_\odot$ and for particle-based codes, $m_{\text{gas,ic}} = 6.86 \times 10^4 M_\odot$. Dark matter distributions of these runs at the final redshift ($z = 10$) are shown in Figure 1.

We adopt a new refinement scheme to ensure consistent physical resolution between the *High-z Run* and the *CosmoRun* simulations. In the *High-z Run*, mesh-based codes reach the finest cell size of 348 comoving pc, while particle-based codes use gravitational softening lengths of 1600 comoving pc until $z = 19$ where the first star emerges, and 80 physical pc thereafter. This strategy yields a uniform physical resolution of 22 – 32 pc during the peak star formation epoch, a spatial resolution that corresponds to the epoch when star formation actively occurs in the *CosmoRun*. The 1600 comoving pc for the particle-based code is set to be in accordance with the mesh-based codes, which have a comoving length twice as large compared to the *CosmoRun* at $z \geq 19$.

2.3. SKIRT Radiative Transfer Code

We utilize the radiative transfer code SKIRT (Camps & Baes 2020) to generate mock images and estimate the UV luminosity of our simulated galaxies, accounting for both dust attenuation and emission.

Each galaxy’s radiation sources are represented by star particles within the halo. For every stellar particle inside R_{vir} , we imported the positions, initial masses, smoothing lengths, metallicities, and ages directly from the simulation outputs. The initial stellar masses were either derived from the stellar mass loss routines of the respective simulation codes or obtained from explicitly provided stellar mass data in each code. To determine the smoothing length for each star particle, we calculated the distance to its 32nd-nearest neighboring star particle with an upper limit of 80 pc. We divide

stellar populations into two groups to include star-forming nebular emission, as nebular emission is an important indicator in measuring galaxy properties at high redshift in the limited available wavelength. For the older stellar population, we adopted the Binary Population and Spectral Synthesis (BPASS) model of Stanway & Eldridge (2018), utilizing a Chabrier (2003) initial mass function (IMF) to define the stellar emission properties. For young stellar particles (ages ≤ 30 Myr), the TODDLERS library (Kapoor et al. 2023) is employed. Coupled with a semi-analytical gas-cloud evolution model, the TODDLERS library produces a spectral energy distribution (SED) that includes stellar continuum, dust emission, nebular continuum, and line emission from both H II and molecular gas regions. In these models, we assumed a nebular density of $n_{\text{H}} = 100 \text{ cm}^{-3}$ following Ceverino et al. (2019) and a star formation efficiency of $\epsilon_{\text{SF}} = 0.1$, higher than that in the local universe, allowing the disruption of clouds (Kapoor et al. 2023).

The interstellar medium (ISM) in our simulations is modeled according to the output format specific to each code: grid-based structure for ENZO, and RAMSES, and particle-based representations for CHANGA, GADGET-3, GADGET-4, and GIZMO. The dust distribution is proportional to the gas density, with the condition that dust formation occurs only in gas elements with temperatures below $T_{\text{max}} = 15000 \text{ K}$, assuming that dust is destroyed at $T \geq 15000 \text{ K}$ (Paper VIII). The dust density (ρ_{dust}) is calculated using the following relation:

$$\rho_{\text{dust}} = \begin{cases} f_{\text{dust}} Z_{\text{gas}} \rho_{\text{gas}} & \text{if } T < T_{\text{max}} \\ 0 & \text{otherwise} \end{cases}$$

Where ρ_{dust} and ρ_{gas} are the densities of dust and gas, respectively. Z_{gas} is the gas metallicity fraction and f_{dust} is the dust-to-metal (DTM) ratio. Considering that dust production is inefficient at high redshift (Behrens et al. 2018) and the decrease in the dust-to-metal ratio toward higher redshift (Heintz et al. 2023), we adopt a value of $f_{\text{dust}} = 0.1$, which is relatively low compared to that in the local universe of 0.2 – 0.5 (De Vis et al. 2019; Konstantopoulou et al. 2024).

In the observed spectra of high-redshift objects, the Gunn–Peterson trough (Gunn & Peterson 1965) arises from absorption of Lyman- α photons by neutral hydrogen in the intergalactic medium (IGM), producing a broad region of zero flux at wavelengths shorter than the Lyman lines. Because SKIRT does not include IGM absorption along the line of sight, this effect is mimicked by setting the flux to zero at wavelengths shorter than the Lyman- α line corresponding to the source redshift.

2.4. Participating Codes

Here, we provide a brief introduction to the numerical codes that participate in the *High-z Run* and their applica-

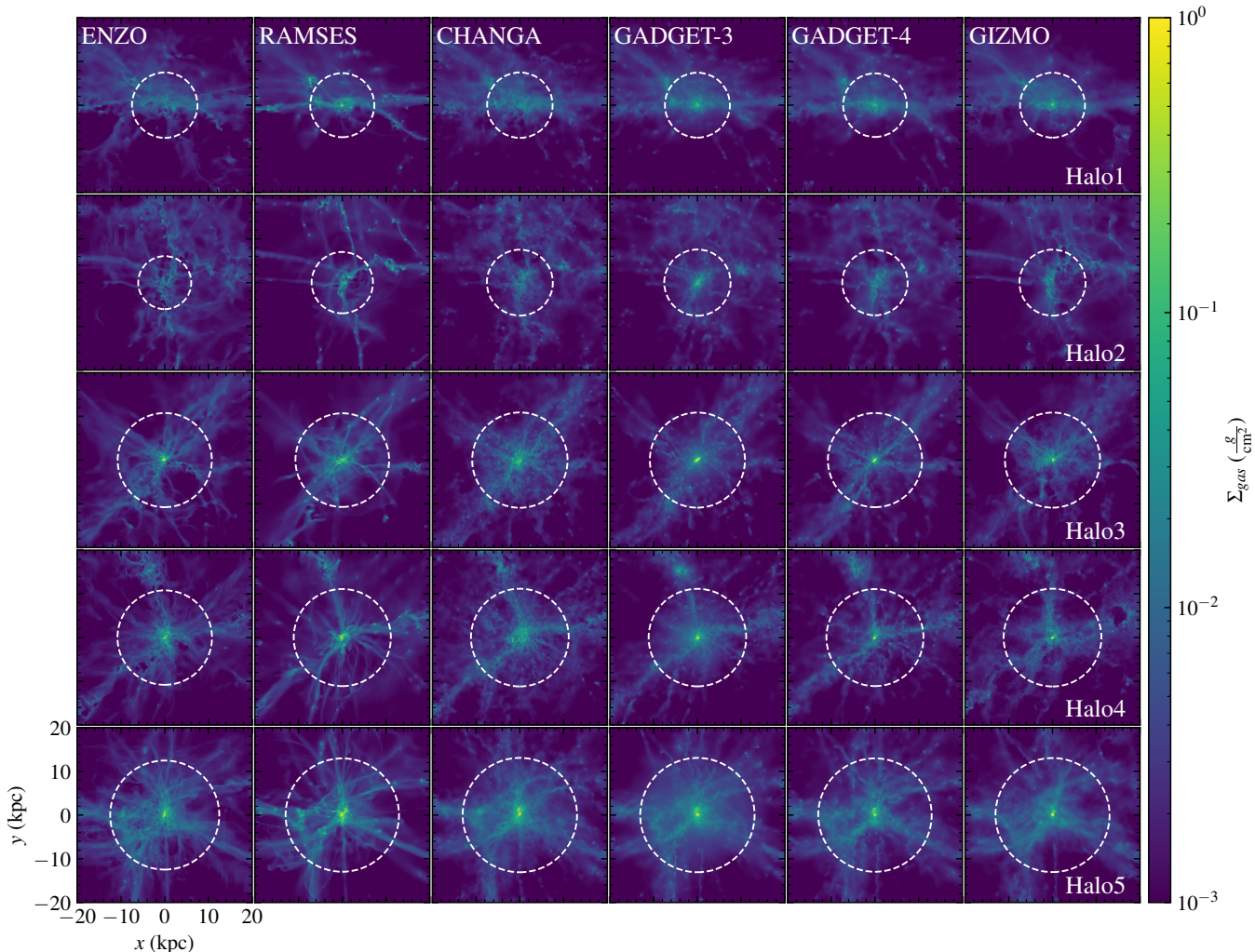


Figure 2. Gas density projections at $z = 10$ from the *High- z Run* for the five target halos. The virial radius of each target halo is indicated by a white dashed circle. While the participating codes show good overall agreement in gas distribution, some inter-code differences in the gas concentration in the circumgalactic region are notable. See Section 3.1 for more information.

tions to high-redshift galaxy studies if available. It should be noted that the participating codes do not represent their entire code communities, as differences in parameter choices and subgrid physics can exist even within a single code. However, for clarity, we refer to each participating code by its code name. Previous *AGORA* papers have presented comprehensive descriptions of each code: gravity solvers (Paper I), hydrodynamic solvers (Paper II), stellar feedback implementations (Papers III and IV). Therefore, we refer interested readers to these papers for full technical details.

2.4.1. ENZO

ENZO (Bryan et al. 2014) is a block-structured AMR code. Originally developed by Greg Bryan and later released as a publicly available code, it is now actively maintained and extended by a broad collaboration of developers. ENZO employs the stochastic star formation prescription commonly

adopted in the *AGORA* project and models stellar feedback through thermal energy injection from Type II supernovae. Renaissance simulation (McCaffrey et al. 2023) uses ENZO to model galaxy formation in the early universe, finding that the properties of the most massive galaxies in the simulations are consistent with JWST observations.

2.4.2. RAMSES

RAMSES (Teyssier 2002) is also an AMR code that uses a tree-based grid structure to solve the gravity and hydrodynamic equations. In this paper, RAMSES adopts the delayed-cooling thermal feedback model introduced by Dubois et al. (2015), which locally delays the gas cooling after an explosion. Also, it considers only the thermal energy input from Type II supernovae as stellar feedback. Andalman et al. (2025) investigates the mechanisms that drive massive galaxy

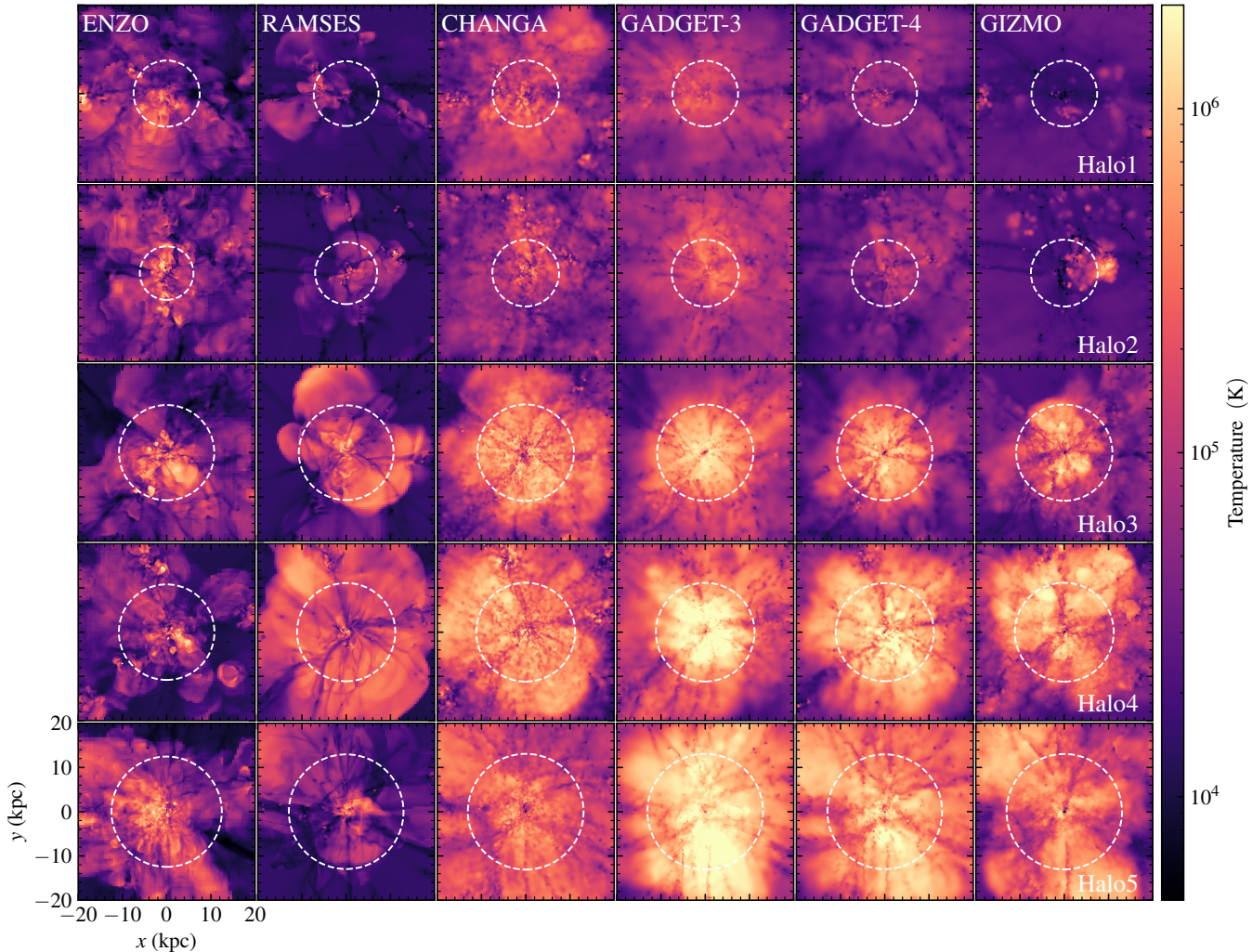


Figure 3. Density-weighted projections of gas temperature at $z = 10$ from the *High- z Run* for the five target halos. Similar to Figure 2, white circles indicate the virial radius of the halo. As discussed in Paper VI, the adaptive mesh refinement (AMR) codes ENZO and RAMSES exhibit stronger contrast between the cold, high-density clouds and the hot, low-density bulk when compared to the smoothed particle hydrodynamics (SPH) codes in the circumgalactic medium (CGM). See Section 3.1 for more information.

formation at Cosmic Dawn using RAMSES, focusing on the star formation efficiency of galaxies.

2.4.3. CHANGA

CHANGA (Menon et al. 2015) is an SPH code built on the Charm++ parallel programming framework. Reimplemented from the earlier SPH code GASOLINE (Wadsley et al. 2017), it employs a k -th nearest neighbor algorithm with $N_{\text{ngb}} = 64$ for both gravitational and hydrodynamic calculations. For the *High- z Run*, CHANGA adopts the “superbubble” feedback model, which introduces a small, hot region around supernova events to capture their nature (Keller et al. 2014). In this study, we follow the same stellar feedback prescription used in Paper III, but use 3.25×10^{51} erg/SN instead of 5×10^{51} erg/SN, which is revised in Paper IV. Using CHANGA, van Donkelaar et al. (2025) conducts the PHOE-

BOS simulation, suggesting that a weak stellar-feedback prescription can successfully reproduce galaxy properties at $z \geq 8$.

2.4.4. GADGET-3

GADGET-3-OSAKA is a modified version of the SPH code GADGET-3, enhanced with a suite of subgrid physics modules for star formation and feedback developed by the Osaka group. Its prescriptions follow Aoyama et al. (2017); Shimizu et al. (2019), implementing both thermal and kinetic feedback. Feedback energy is injected into the surrounding particles through a hot-bubble scheme with a time delay, where the delay time and bubble size depend on local gas density and pressure, and the feedback energy. Chemical enrichment is modeled using metal yields from the chemical evolution library CELib (Saitoh 2017). Jeong et al. (2025)

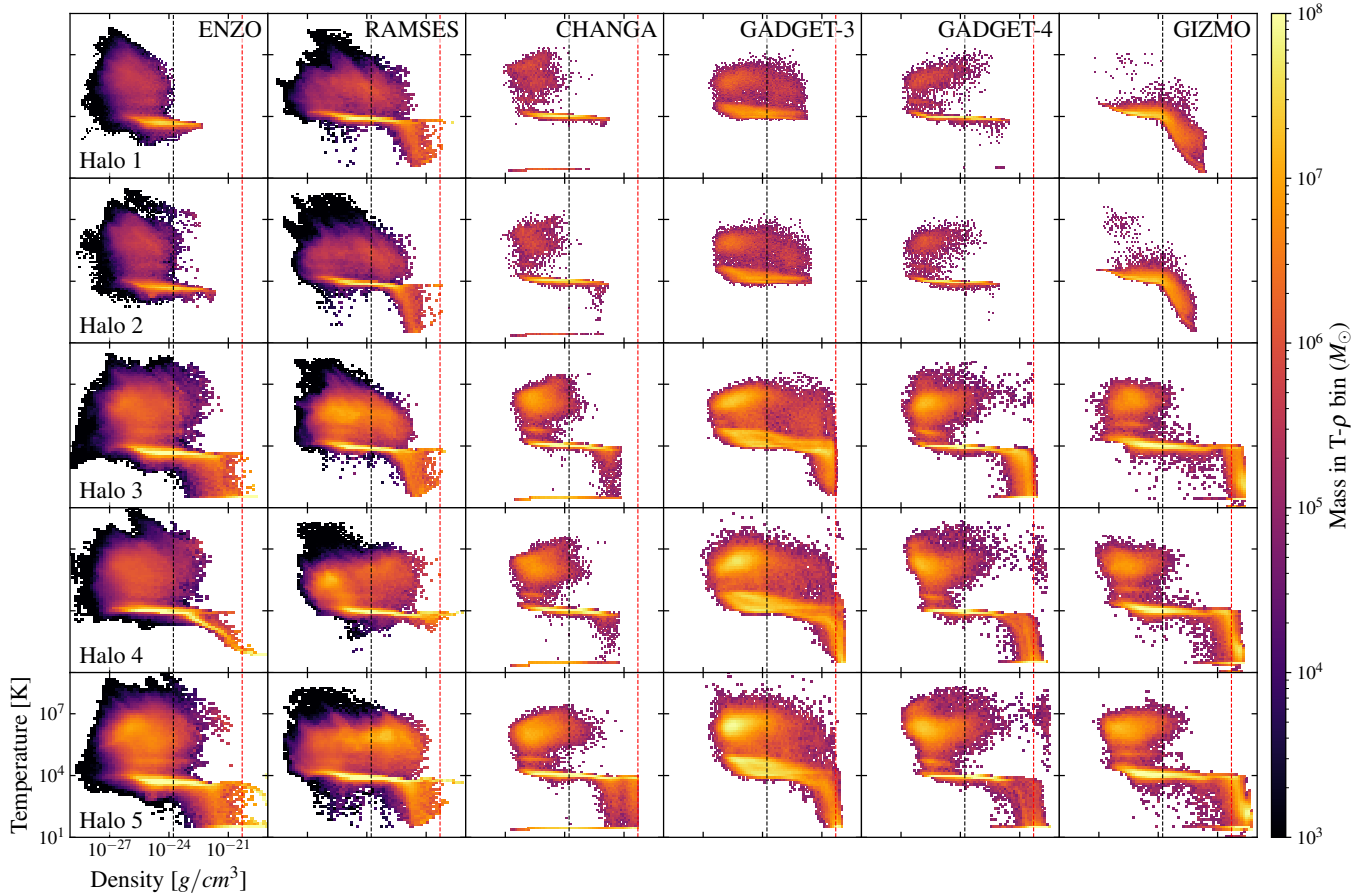


Figure 4. Two-dimensional probability distribution functions (PDFs) of gas density and temperature at $z = 10$ in the *High-z Run*. Gas within the R_{vir} of the halos is included, with the color representing the total gas mass in each bin. Star formation density threshold ($n_{\text{H}} = 1 \text{ cm}^{-3}$) and feedback-free starbursts (FFB) density threshold ($n_{\text{H}} = 3000 \text{ cm}^{-3}$) are annotated as vertical black and red dashed lines, respectively. Halos with virial masses above the FFB mass threshold ($M_{\text{halo}, z=10} = 3.5 \times 10^{10} M_{\odot}$; Halos 3, 4, and 5) contain denser gas than halos below the threshold. RAMSES consistently produces very dense gas regardless of halo mass, in contrast to other codes. See Section 3.1 for more information.

conducts cosmological hydrodynamic zoom-in simulations in a high redshift environment with a top-heavy IMF and star formation efficiency using GADGET-3.

2.4.5. GADGET-4

In the *High-z Run*, we add the results of the GADGET-4 (Springel et al. 2021) code using the GADGET-4-OSAKA model. GADGET-4-OSAKA is also a modified version of the SPH code GADGET-4, incorporating an updated stellar feedback model (Oku et al. 2022) and AGN physics developed by the Osaka group (Oku & Nagamine 2024). It also supports delayed cooling and feedback implemented through two distinct channels, a local mechanical feedback and a large-scale hot galactic wind component. The mechanical feedback injects the terminal momentum of unresolved supernova remnants calibrated from high-resolution simulations, while the wind model captures the large-scale expulsion of hot gas. The detailed calibration steps of GADGET-4 in the *CosmoRun* are presented in the Appendix of Paper VIII.

2.4.6. GIZMO

GIZMO (Hopkins 2015) is a hybrid code that bridges particle-based and grid-based methods through a fully Lagrangian hydrodynamics solver. It supports multiple schemes, including meshless finite mass (MFM) and meshless finite volume (MFV), allowing flexible treatment of fluid dynamics. In the *High-z Run*, the MFM method is adopted. The stellar feedback model follows the FIRE-2 model Hopkins et al. (2018), distributing both kinetic and thermal energy and metals to neighboring particles through kernel-weighted schemes. The FIRE-2 galaxy formation model Hopkins et al. (2018) has been implemented into GIZMO and applied to the study of high-redshift galaxies, including investigations of star formation and UV luminosity from the FIRE-2 and FIREbox^{HR} cosmological simulations (Sun et al. 2023; Feldmann et al. 2025). Please note that although the GIZMO in the *High-z Run* adopts the FIRE-2 stellar feedback prescription, it does not represent the FIRE-2 model, as many other aspects (e.g., star formation model, cooling algorithm)

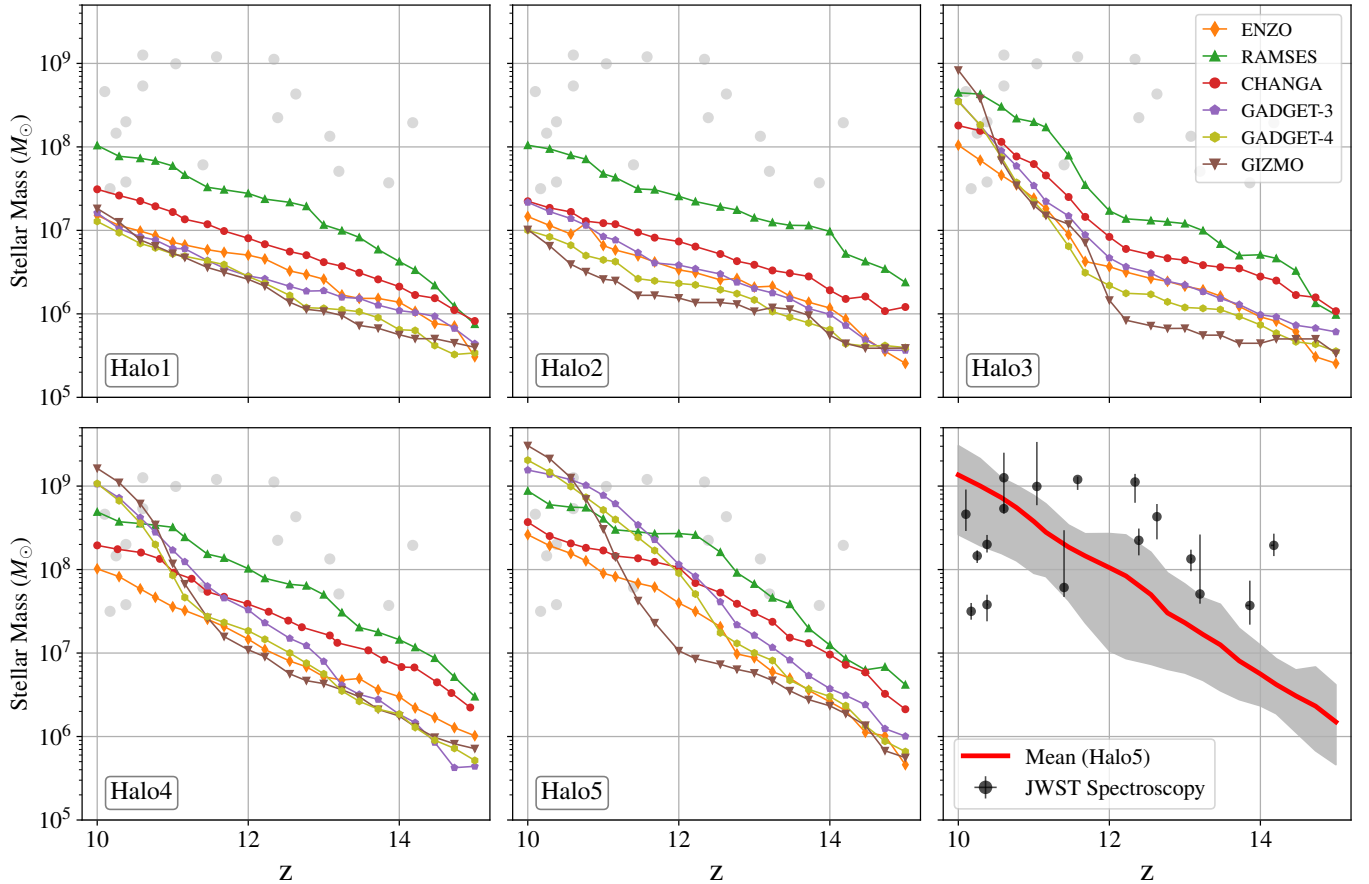


Figure 5. Evolution of stellar mass histories in the *High-z Run*. Each panel shows the results for a different target halo. Stellar mass is calculated as the total stellar mass within R_{vir} of the halo, following the methodology adopted for Figure 4 in Paper IV. To compare with observations, in the bottom right panel we present the mean value (thick red line) and the minimum–maximum range (gray shaded region) of Halo 5 and JWST observation data (black dots with error bars) from the following works: Bunker et al. (2023); Tacchella et al. (2023); Wang et al. (2023); Harikane et al. (2024); Hsiao et al. (2024); Robertson et al. (2024); Carniani et al. (2025); Wu et al. (2025). The observation data points are replicated in other panels as translucent gray dots. Despite some variations in stellar mass across simulations, the *High-z Run* Halo 5 results show good agreement with observations, reproducing similar stellar masses except at $z \sim 14$. See Section 3.2 for more information.

differ significantly from those in the original FIRE-2 framework.

3. RESULTS

3.1. Gas Properties

Figure 2 presents the projected gas density of each halo in the *High-z Run*. Each panel spans 40 kpc in physical scale, with dashed white circles marking the virial radii. While the participating codes broadly agree on the overall gas distribution, inter-code differences emerge in the compactness of the gas. GADGET-3, GADGET-4, and GIZMO show highly compact cores at the halo centers, whereas mesh-based codes maintain more diffuse gas in the CGM.

Figure 3 shows the corresponding density-weighted temperature maps for the same regions. Here, the differences are even more pronounced. Particle-based codes generate hotter central regions and extended, smooth temperature gradients, while mesh-based codes produce sharper contrasts be-

tween cool, dense clumps and the hot, low-density CGM. This result is consistent with findings in Paper VI. Mesh-based codes inject energy into a single cell and then spread it into the surrounding area, whereas particle-based codes distribute feedback energy to neighboring particles, producing a more extended hot region than mesh-based codes.

These figures highlight that, unlike the dark matter distribution (Figure 1), the gas density and thermal structure exhibit clear inter-code variations that arise from the different numerical solvers of each simulation framework.

To investigate the details of gas properties, Figure 4 presents the density–temperature probability distribution function (PDF) at $z = 10$ for gas within R_{vir} of halos, with the star formation density threshold ($n_{\text{H}} = 1 \text{ cm}^{-3}$, vertical black dashed line) and density threshold ($n_{\text{H}} = 3000 \text{ cm}^{-3}$, vertical red dashed line) proposed from FFB scenario (Dekel et al. 2023). First, we can see that the physics of the *CosmoRun* is clearly reflected in the *High-z Run*. (For the de-

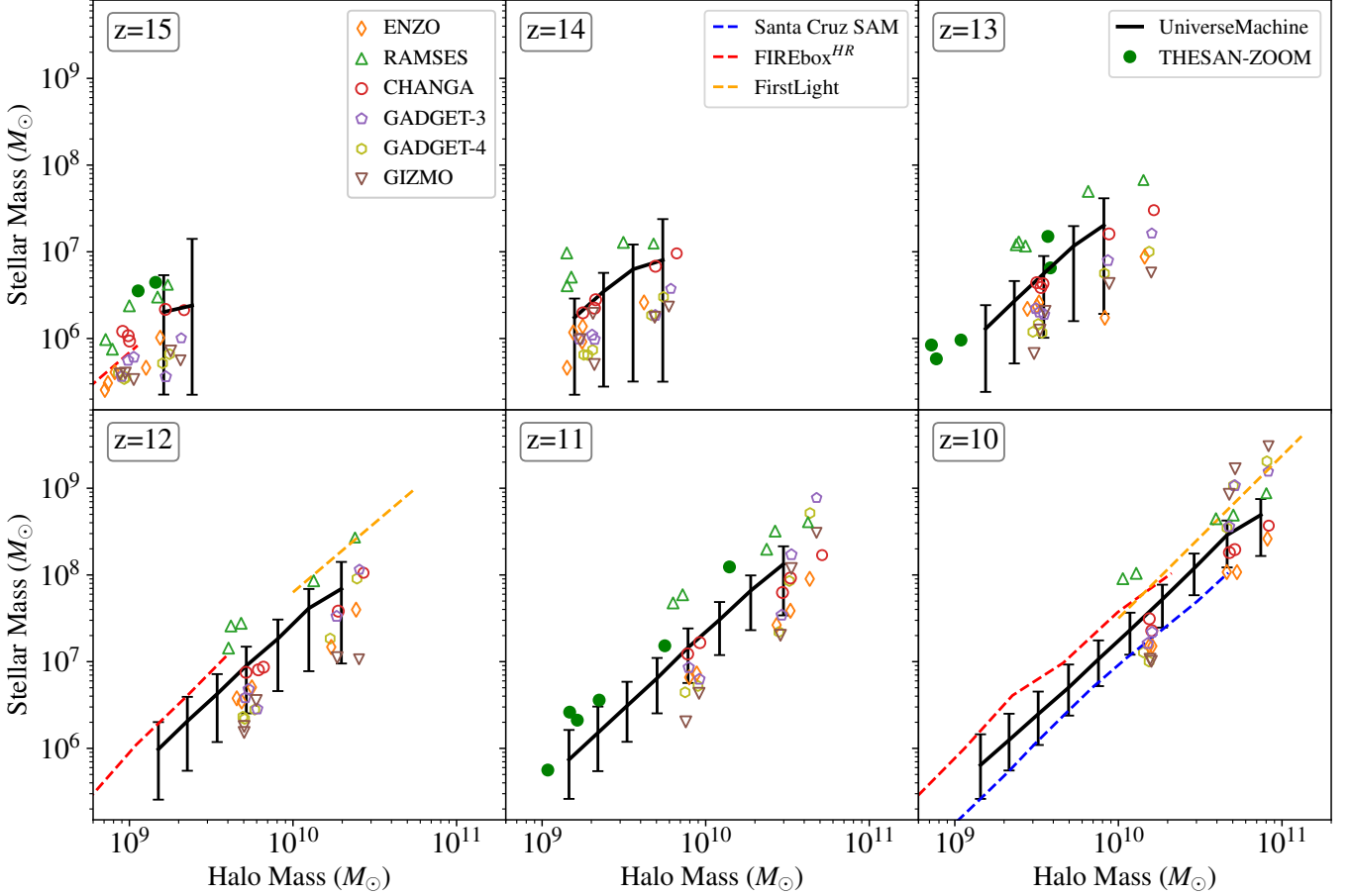


Figure 6. Evolution of the stellar mass-halo mass (SMHM) relation of the galaxies in the *High-z Run*. The galaxies in the *High-z Run* are marked with an open colored symbol at selected epochs. For comparison, we display the estimates from abundance matching techniques UniverseMachine (Behroozi et al. 2020, black solid line with error bar) and semi-analytic model Santa Cruz SAM (Yung et al. 2019, blue dashed line at $z = 10$, 12, and 15). We also present the SMHM relation in other cosmological simulations, FIREbox^{HR} (Feldmann et al. 2025, red dashed line at $z = 10, 11, 13, \text{ and } 15$), FirstLight (Ceverino et al. 2024, orange dashed line at $z = 10, 12$) and THESAN-ZOOM (Kannan et al. 2025, green dots at $z = 10$). Most of the *High-z Run* galaxies align with the previous works, but some galaxies have slightly higher stellar mass at $z = 10$. See Section 3.2 for more information.

tails, see Figure 14 of Paper III). (1) the black bins at low-density and high-temperature regions in mesh-based codes, which come from the small mass gas cells in the CGM. (2) high density and hot gas phase above the star formation threshold due to delayed-cooling in RAMSES, GADGET-3, and GADGET-4. (3) cooling curve at $\sim 10^4$ K, where gas cooling rate balances the heating rate in the CLOUDY table. Nevertheless, there are also differences between the *High-z Run* and *CosmoRun*. Since the target halos of the *High-z Run* have very massive halo mass already at extremely high-redshift, gas is concentrated rapidly, which results in a very dense gas region above the star formation threshold. Especially, Halos 3, 4, and 5 have very dense and cold gas ($\sim 10^{-21} \text{ g/cm}^{-3}$, 10^2 K), which is not shown in Halos 1 and 2. Also, GADGET-3, GADGET-4, and GIZMO show a significant amount of cold dense gas compared to the other codes. At high redshift, accretion in halos is dominated by

cold streams from dense filaments despite the presence of a hot surrounding CGM. In these flows, the cooling time is shorter than the compression heating time from the virial shock (Dekel & Birnboim 2006), preventing the formation of a stable shock. This allows cold gas to penetrate into the hot CGM and sustain inflowing streams into the halos. Moreover, the host masses of Halos 3, 4, and 5 exceed the mass threshold ($M_{\text{halo}} = (1+z)^{-6.2} 10^{17} M_{\odot}$, $3.5 \times 10^{10} M_{\odot}$ at $z = 10$) proposed by Dekel et al. (2023), leading to the very dense gas reservoirs ($n_{\text{H}} \sim 3000 \text{ cm}^{-3}$), where the stellar feedback becomes inefficient.

RAMSES consistently produces such dense gas cells regardless of halo mass. This feature comes from the refinement strategy of RAMSES implemented in the *CosmoRun* suite. RAMSES extends the high-resolution region around the dense cells to avoid discontinuity of resolution between the high density region and the nearby lower density regions. As

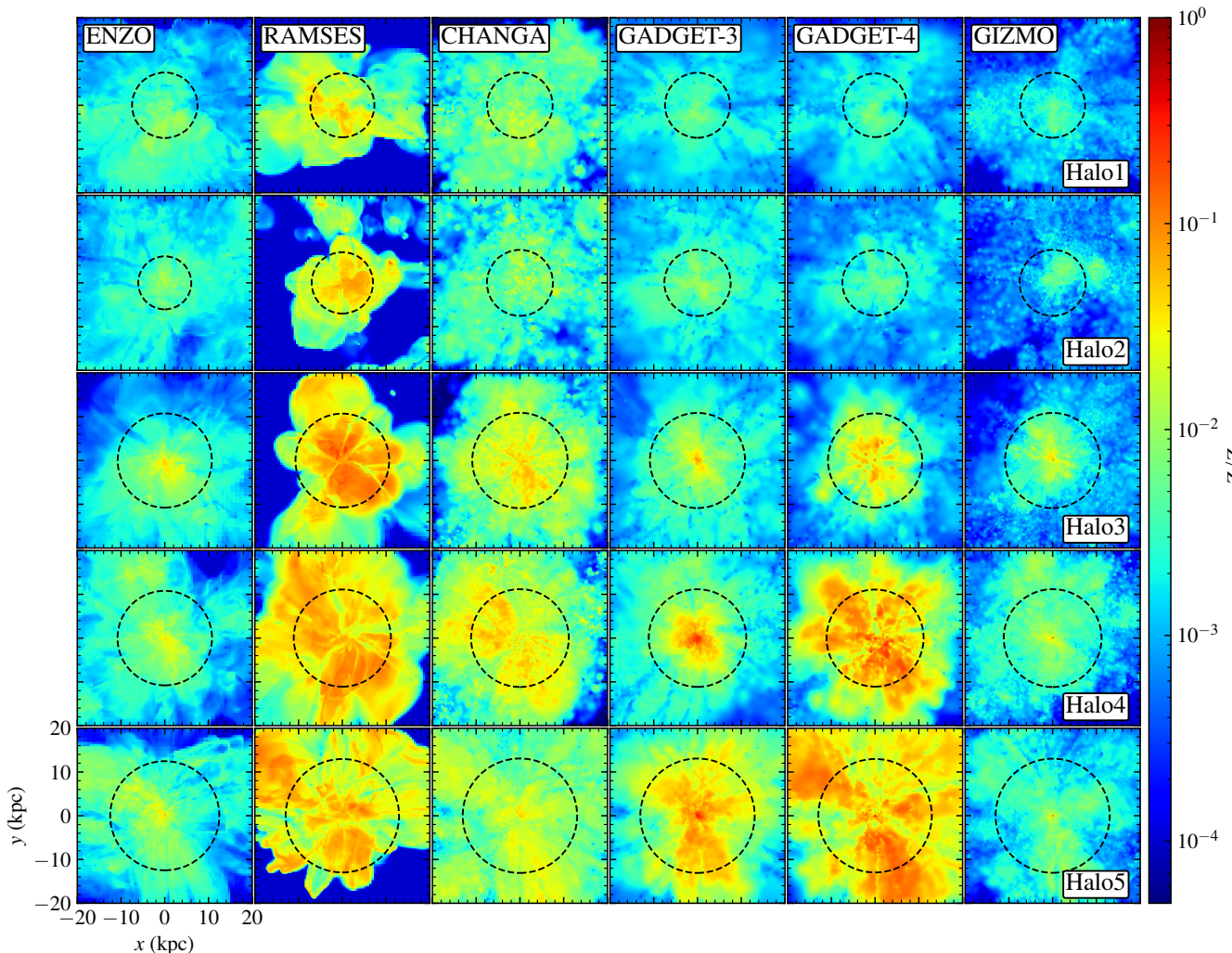


Figure 7. Density-weighted projections of gas metallicity at $z = 10$ from the *High- z Run* for the five target halos. As in Figures 2 and 3, the black circles indicate the virial radius of the halos, and the color scale represents gas metallicity in units of Z_{\odot} . Although the total gas mass within the virial radius is comparable across codes, metal distributions differ significantly. See Section 3.3 for more information.

a consequence, RAMSES has a more extended and refined region, compared to the other codes.

3.2. Stellar Mass Evolution

Figure 5 shows the stellar mass growth histories of halos as functions of redshift. Stellar mass is measured within the virial radius (R_{vir}), centered on each halo. The difference between participating codes tends to broaden as the host halo mass increases. Codes show very good agreement within less than 0.5 dex in Halo 1 except RAMSES, but inter-code differences grow to ~ 1 dex in Halo 5. This trend is expected, as halo mass reflects the depth of the gravitational potential well at the galaxy center. The deep potential well of Halo 5 enables more efficient gas accretion from the IGM and sustains higher star formation, which results in various star formation histories from different stellar feedback across codes. Previous studies (Hayward & Hopkins 2017; Kang et al. 2025)

show that different stellar feedback recipes can affect star formation at high redshift. Looking at some individual codes, RAMSES consistently produces higher stellar masses in the early stages regardless of the halo mass. These results come from its refinement strategy, which achieves a more extended maximum spatial resolution than other codes. For example, ENZO and RAMSES are both mesh-based code, the number of the finest cells differs at $z = 15$ by a factor of 4 in the center of the galaxy. Despite this early disparity, RAMSES converges to comparable stellar masses at the final redshift when the structures collapse and the star forming region becomes dense enough for star formation in all codes.² GIZMO

² We note that the star formation of RAMSES at higher redshift ($z \sim 15$) is highly sensitive to the refinement strategy choice, but reaches similar stellar mass at $z \sim 10$. In the future study, we will investigate the effect of refinement at high redshift, when the first stars are formed.

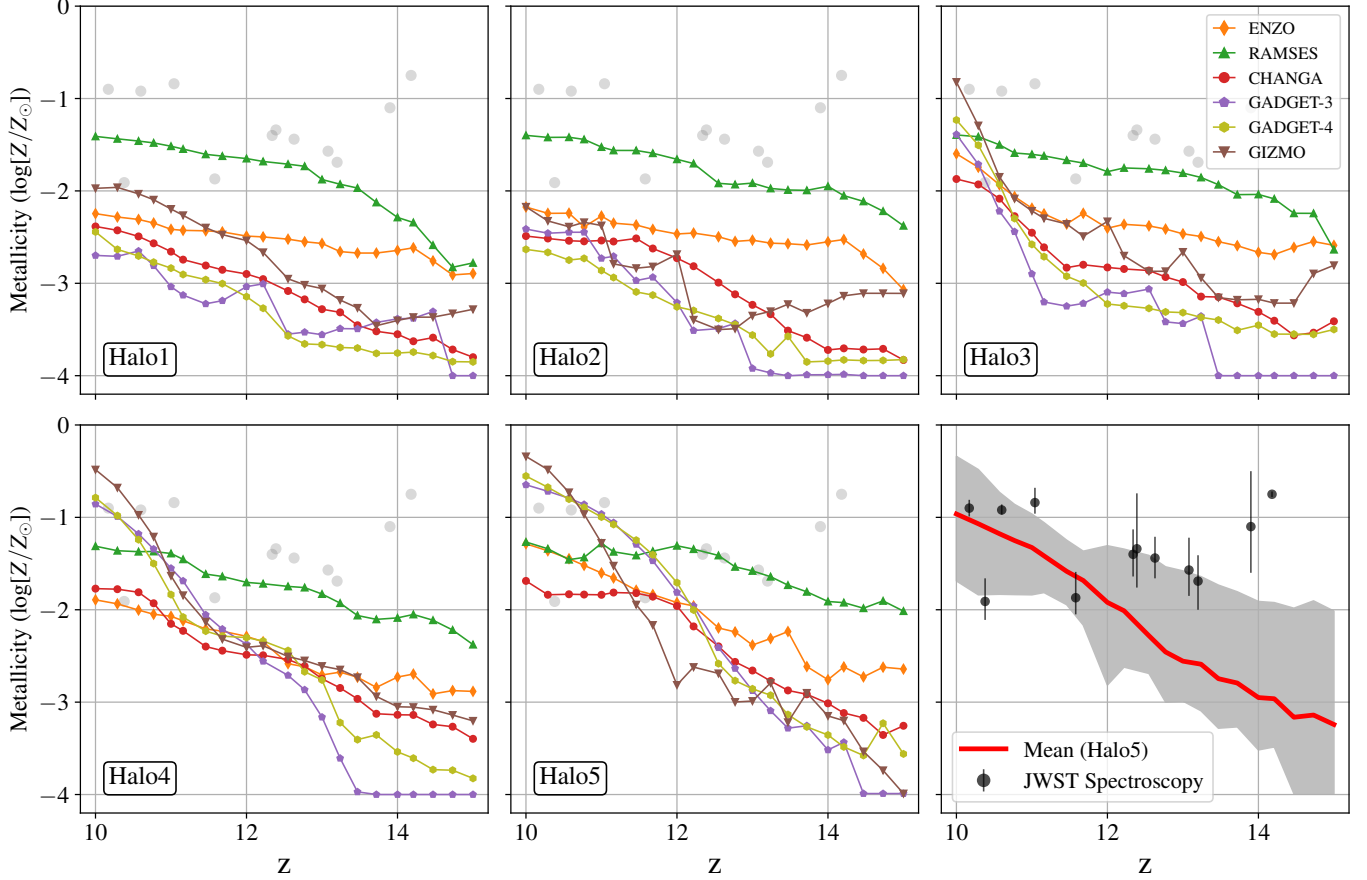


Figure 8. Metallicity evolution histories in the *High-z Run* as a function of redshift. Metallicity is defined as the mass-weighted metallicity of star particles younger than 100 Myr, assuming young star particles share the metallicity of their star-forming regions. Metallicity exhibits larger inter-code variations than stellar mass. To compare with observations, in the bottom right panel we present the mean value (thick red line) and the minimum–maximum range (gray shaded region) of Halo 5 and the JWST observation data (black dots with error bars) from the following works: [Bunker et al. \(2023\)](#); [Curtis-Lake et al. \(2023\)](#); [Wang et al. \(2023\)](#); [Hsiao et al. \(2024\)](#); [Castellano et al. \(2024\)](#); [Carniani et al. \(2025\)](#); [Wu et al. \(2025\)](#). The observation data points are replicated in other panels as translucent gray dots. The *High-z Run* reproduces the observed metallicity at $z < 12$, but underpredicts at higher redshift, with the exception of RAMSES. See Section 3.3 for more information.

exhibits distinctive sensitivity to merger events. While Halos 3 and 4 have similar final halo masses, Halo 3 starts a major merger (mass ratio $\sim 1 : 1$) around $z \sim 12$, leading to a pronounced increase in stellar mass for GIZMO afterward. This is also observed in the other codes, but GIZMO shows the rapid stellar mass increase.

Overall, the tendency of stellar mass growth is similar across the simulation codes, but ~ 1 dex of inter-code differences exist throughout the redshift range. However, compared to the stellar mass assembly history (SMAH) presented in Paper III, the *High-z Run* shows better convergence at $z = 10$ with a similar stellar mass range (~ 1.5 dex in the *CosmoRun* and ~ 1 dex in the *High-z Run*). We also conduct an additional run with different feedback strengths and found that convergence is driven more by differences in feedback models between codes than by variations in feedback energy strength within a single code (see Appendix A for detail). From these results, we conclude that the simulation codes

converge well, although they are calibrated at a relatively low redshift ($z = 4$).

We also compared our results to the spectroscopically confirmed JWST observation data ([Bunker et al. 2023](#); [Tacchella et al. 2023](#); [Wang et al. 2023](#); [Harikane et al. 2024](#); [Hsiao et al. 2024](#); [Robertson et al. 2024](#); [Carniani et al. 2025](#); [Wu et al. 2025](#)). In the bottom-right panel, we present the high-redshift galaxies from JWST observation as black dots with error bars, and the red line and gray shaded region represent the mean values and minimum-maximum values of the six participating codes from Halo 5. Without changing the sub-grid physics for low redshift, the *High-z Run* can reproduce the stellar mass at $z < 12$ from JWST observation data, but it is insufficient for higher redshifts above that.

The stellar mass–halo mass (SMHM) relation is a fundamental relation of galaxy evolution that quantifies the efficiency of star formation in the host halos ([Moster et al. 2010](#)). Figure 6 presents the evolution of the SMHM rela-

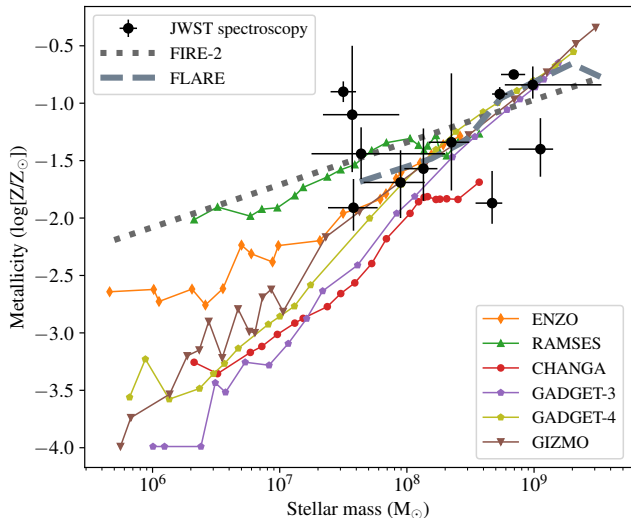


Figure 9. The stellar mass–metallicity relation (MZR) from the *High-z Run*. We present MZR evolution of Halo 5, alongside JWST observational data points (black dots with error bars, Bunker et al. 2023; Curtis-Lake et al. 2023; Wang et al. 2023; Hsiao et al. 2024; Castellano et al. 2024; Carniani et al. 2025; Wu et al. 2025). We also include the gas-phase mass-metallicity relation from the FIRE-2 simulation (gray dotted line, Marszewski et al. 2024) and FLARE simulation (gray dashed line Wilkins et al. 2023). The participating codes diverge at the low-mass end, but converge well at higher mass, showing good agreement with observations and other cosmological simulations. See Section 3.3 for more information.

tion of the *High-z Run* during $z = 15 - 10$. For comparison, we also compare our work to other theoretical models and simulations. These include the semi-empirical model UniverseMachine (solid black line, Behroozi et al. 2020), the semi-analytic model Santa Cruz SAM (blue dashed line, Yung et al. 2019), and simulations from FIREbox^{HR} (red dashed line, Feldmann et al. 2025), FirstLight (orange dashed line, Ceverino et al. 2024), and THESAN-ZOOM (green dots, Kannan et al. 2025). The *High-z Run* results are marked with open symbols, and we represent the median (Santa Cruz SAM) and average values (FIREbox^{HR} and FirstLight) of previous studies as dashed lines for comparison. Across the redshift range, our results are consistent with previous studies. Except for RAMSES, the participating codes show good convergence below $M_{\text{halo}} \sim 10^{10} M_{\odot}$, but begin to diverge toward lower redshifts, with differences of up to about 1 dex. Nevertheless, the overall trends in the *High-z Run* remain in broad agreement with earlier works.

3.3. Metallicity Properties

Figure 7 shows the density-weighted gas metallicity projections for the five halos across six simulation codes. While the overall gas distributions are broadly similar, the metallicity patterns exhibit clear differences. In Halos 1 and 2, only RAMSES reaches significantly higher metallicity than

the other codes due to its higher star formation in low-mass halos, which enhances early metal enrichment. For Halos 3, 4, and 5, the divergence among codes becomes more pronounced, reflecting the distinct outflow behaviors discussed in Paper VI. In Paper VI, RAMSES, CHANGA, and GADGET-3 have strong outflows that mix chemical elements around the galaxy center, while ENZO (very narrow outflow) and GIZMO (weak outflow) do not. Therefore, in the *High-z Run*, the CGM region of the former three codes has higher metallicity, the rest show less enrichment (ENZO), or are concentrated in the center (GIZMO). GADGET-4, which is newly added, shows the most efficient metal enrichment in the CGM. In this study, we do not examine the inflow and outflow characteristics of the *High-z Run* galaxies, this analysis will be conducted in the future AGORA project. These results highlight how differences in the implementation of the star formation and feedback models affect the metal enrichment processes.

Metallicity is an important tracer for estimating galaxy properties such as stellar masses, ages, star formation rates, and redshifts. Figure 8 illustrates metallicity histories in the *High-z Run* as a function of redshift. We follow the definition of galaxy metallicity from Langan et al. (2020), calculating it as the mass-weighted average metallicity of star particles younger than 100 Myr within the virial radius (R_{vir}), under the assumption that these particles share the metallicity of unresolved nebular regions, allowing comparison of our results with observational data. Generally, the metallicity evolution follows the star formation history of each halo, although it shows larger inter-code differences. For example, while GADGET-3 exhibits efficient metal diffusion at $z = 10$ (as shown in Figure 7), but its diffusion is weak at $z \geq 13$ because it does not implement an explicit metal diffusion scheme. Metals spread only via kernel-weighted injection in supernova events, and at very high redshift, metal enrichment is local and the turbulent mixing time can exceed the collapse time, resulting in a distinct plateau around a metallicity floor of $\sim 10^{-4} Z_{\odot}$. In contrast, RAMSES consistently produces higher metallicities at earlier epochs due to its efficient star formation. The other codes (ENZO, CHANGA, GADGET-4, and GIZMO) broadly show agreement, although GIZMO exhibits a rapid increase at $z \leq 11$ in more massive halos.

Observational metallicity data from JWST spectroscopy (Bunker et al. 2023; Curtis-Lake et al. 2023; Wang et al. 2023; Hsiao et al. 2024; Castellano et al. 2024; Carniani et al. 2025; Wu et al. 2025) are also included for comparison in bottom right panel as black dots with the red mean line and the minimum-maximum gray shaded region of Halo 5. Interestingly, RAMSES is exactly in line with the observation data at $z \sim 13$. We cannot directly compare the *High-z Run* result and observation since the halo mass of the observation

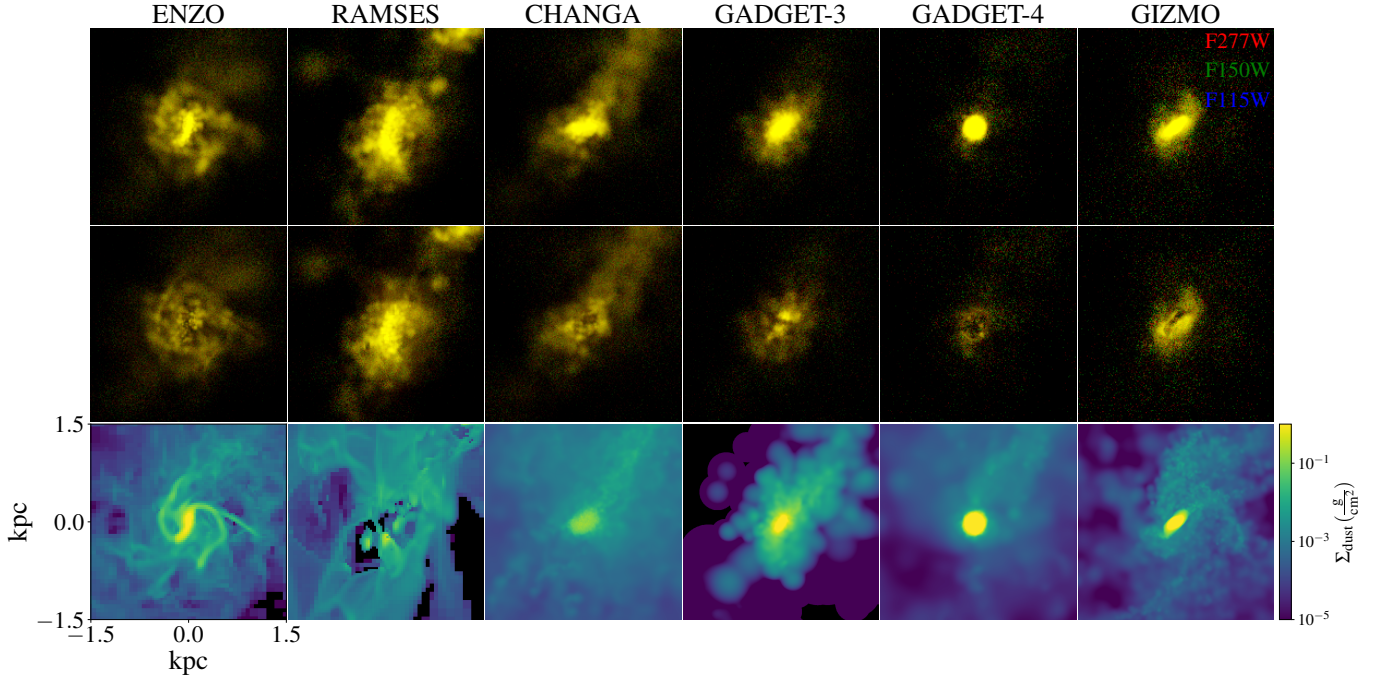


Figure 10. SKIRT-generated mock JWST NIRCам images and dust density projections of Halo 5 at $z = 10$. Three filters (R: F277W, G: F150W, B: F115W) are used as RGB composites. The images are generated from the gas and stellar components within the virial radius R_{vir} . *Upper panels:* Mock image without gas and dust medium. *Middle panels:* Mock image with gas and dust medium. *Bottom panels:* Density projections of dust used to generate mock images. Depending on the dust distribution, dust makes a huge difference in the mock image. See Section 3.4 for more information.

dataset is not known, but this result suggests the possibility of reproducibility of the current galaxy formation model to high-redshift galaxies. At the same time, the rest of *High-z Run* galaxies tend to underpredict metallicity in this regime but generally show good agreement with JWST observations at $z \leq 12$, following similar trends to the star formation histories.

The stellar mass–metallicity relation is known to have a strong positive correlation between stellar mass and metallicity, indicating that more massive galaxies tend to be more metal-enriched (Tremonti et al. 2004). Coupled with the stellar mass, Figure 9 presents the MZR for Halo 5 in the *High-z Run*, compared with JWST spectroscopic measurements and gas-phase MZR of previous cosmological simulations at $z = 10$, FIRE-2 (gray dotted line, Marszewski et al. 2024) and FLARE (gray dashed line, Wilkins et al. 2023). The participating codes show a broad divergence at the low-mass end ($M_* \leq 10^7 M_\odot$), mesh-based codes tend to have higher metallicity than particle-based codes at the low-mass end. However, *High-z Run* galaxies have much better convergence above $10^8 M_\odot$. Although not shown here, this trend is also observed in the other halos and in Paper V. The convergence at higher mass suggests that the dominant chemical enrichment pathways are robust across different simulation methods, while low-mass galaxies remain more susceptible to code-specific differences in the metal diffusion

scheme. Compared with previous simulations, the *High-z Run* galaxies have lower metallicity at the low-mass end and a steeper slope, which comes from different metal enrichment of stellar-phase and gas-phase metallicity at the early stage of galaxy evolution (Mainali et al. 2018). However, at the high-mass end where metal enrichment is sufficiently processed, the differences get smaller and both the *High-z Run* and previous studies show good agreement with JWST spectroscopic observations.

3.4. Mock JWST Image and UV luminosity

Using SKIRT, we generate the mock observation data of simulated galaxies in the *High-z Run*. Figure 10 presents mock JWST NIRCам images of Halo 5 at $z = 10$, generated using the F277W (R), F150W (G), and F115W (B) filters as an RGB composite. The upper panels display images generated from star particles only, while the middle panels additionally include the effects of gas and dust within the virial radius. The lower panels show the projected dust density used in SKIRT. Since we ignore the flux shorter than the Lyman- α wavelength ($\sim 1.3 \mu\text{m}$), the color of galaxies appears yellow. Each pixel corresponds to 17 pc, equivalent to an angular size of about $0.004''$ at $z = 10$ under the same cosmology adopted in the simulations. This resolution is about eight times better than the actual JWST NIRCам resolution ($0.031''$). Images degraded to the JWST resolution, along

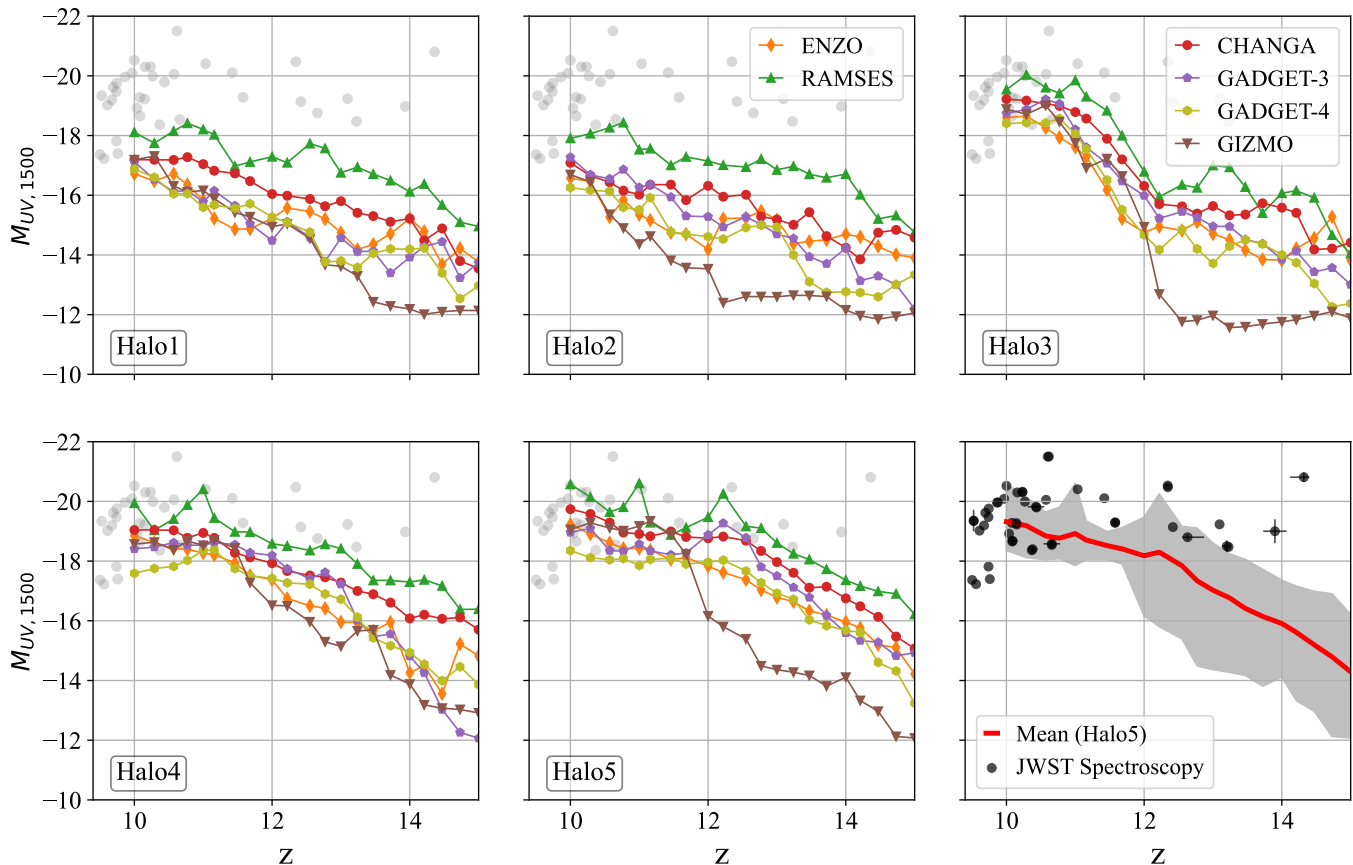


Figure 11. The evolution of UV magnitudes of the *High-z Run* galaxies as a function of the redshift. The UV magnitudes are estimated using the results from the dust-radiative transfer code, SKIRT. To compare with observations, in the bottom right panel we present the mean value (thick red line) and the minimum–maximum range (gray shaded region) of Halo 5 and the JWST observation data — black dots with error bars: Robertson et al. (2023); Bunker et al. (2023); Carniani et al. (2024); Castellano et al. (2024); Napolitano et al. (2025), black dots without error bars: Harikane et al. (2025). The observation data points are replicated in other panels as translucent gray dots. See Section 3.4 for more information.

with clearly visible dust lanes in the rest frame, are presented in the Appendix B. Since the *High-z Run* galaxies do not exhibit a well-defined disk structure, we select the x -axis of the simulation box as the viewing angle. The effect of the medium is evident. While the upper panels illustrate only the stellar distribution, the middle panels display pronounced dark dust lanes resulting from attenuation. The degree of attenuation differs across codes, reflecting variations in the dust density and spatial distribution. For instance, GADGET-4 exhibits a highly concentrated dust core that significantly dims the central region, whereas RAMSES shows weaker attenuation due to its relatively low dust content near the center.

Figure 11 shows the rest-frame UV magnitude at 1500 \AA as a function of redshift, based on our mock observations. The UV flux $f_{UV,1500}$, averaged over the three viewing axes (x , y , z), is converted to absolute magnitude using the relation $M_{UV,1500} = -2.5 \log f_{UV,1500} - 48.6$ (Oke & Gunn 1983), and we confirm that the orientation does not make a big difference in flux. Each panel presents the evolution of UV

magnitude for individual halos from $z = 15$ to $z = 10$. The overall trends closely follow those seen in Figure 5. RAMSES consistently produces brighter magnitudes than the other codes, while GIZMO shows a sharp increase in luminosity following a merger event. To verify the SKIRT results, we compare the UV luminosity histories to the stellar mass histories using the empirical $\log_{10}(M_*/M_\odot) - M_{UV}$ relation at high redshift (Bhatawdekar et al. 2019). The best-fit slope from the *High-z Run* is -0.3 , which is a similar value of -0.4 in Bhatawdekar et al. (2019). Although the relation does not perfectly match the empirical relation, the UV magnitudes from SKIRT simulations show good agreement with the observed scaling relation.

For observational comparison, we include black and gray dots representing spectroscopically confirmed galaxies from JWST observations (Robertson et al. 2023; Bunker et al. 2023; Carniani et al. 2024; Castellano et al. 2024; Napolitano et al. 2025; Harikane et al. 2025). The red mean line and gray minimum-maximum region of Halo 5 are also in-

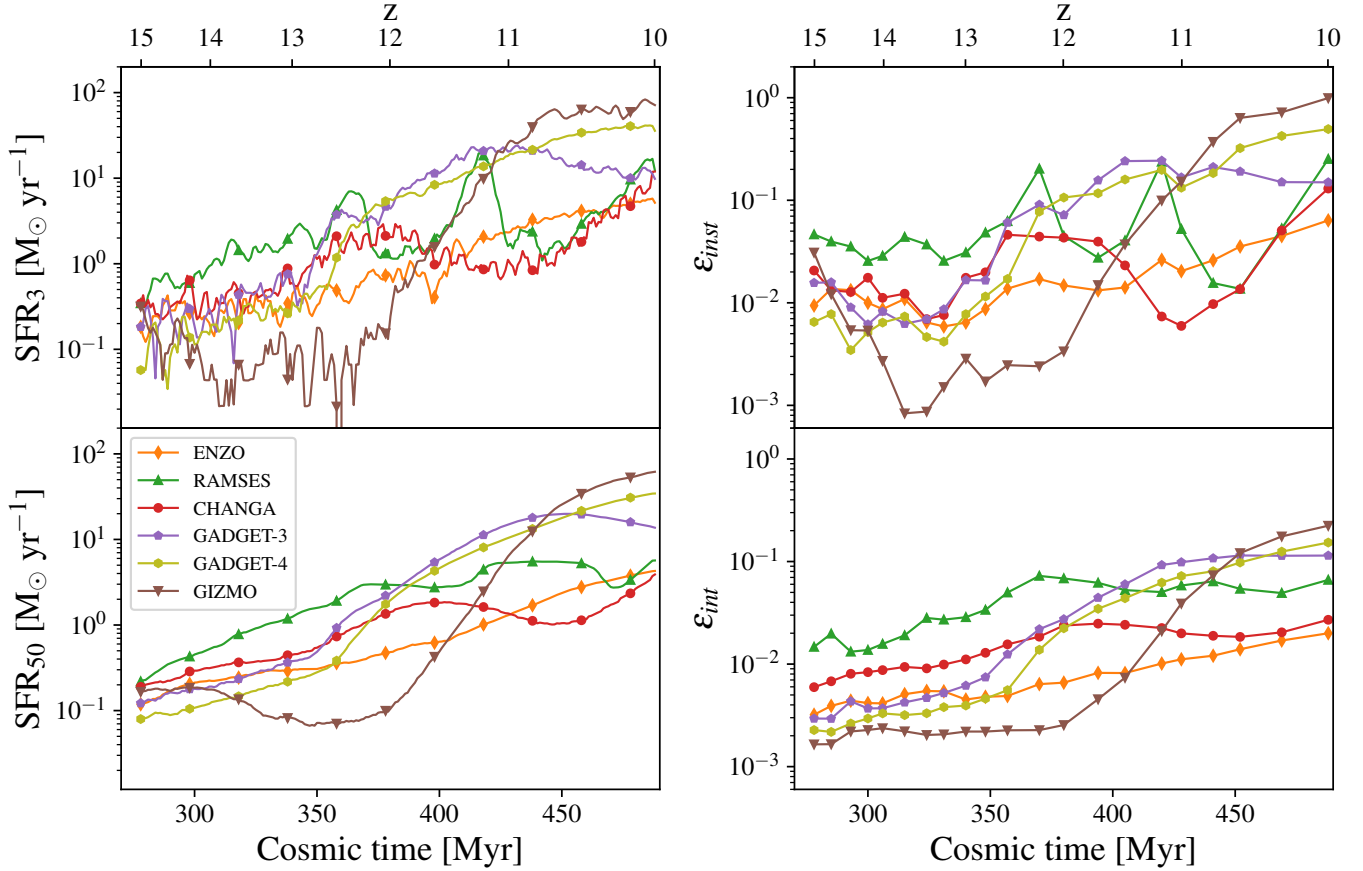


Figure 12. *Upper left panel:* Star formation rate (SFR) of Halo 5 as a function of time, averaged over 3 Myr. *Bottom left panel:* Same as the upper left panel, but averaged over 50 Myr. *Upper right panel:* Instantaneous star formation efficiency, $\epsilon_{\text{inst}} = \dot{M}_*/(\dot{M}_{\text{vir}}f_b)$ at multiple redshifts. *Bottom right panel:* Integrated star formation efficiency, $\epsilon_{\text{int}} \equiv M_*/(M_{\text{vir}}f_b)$. All codes exhibit an overall increasing trend in all panels. See Section 4.1 for more information.

cluded, as in Figures 5 and 8. Our analysis indicates that a halo mass exceeding $5 \times 10^{10} M_{\odot}$ is generally required to match the observed UV brightness. None of the codes in Halos 1 and 2 reproduce the luminosity of observed galaxies, whereas Halos 3, 4, and 5 partially achieve comparable UV magnitudes.

4. DISCUSSION

4.1. Star Formation at Cosmic Dawn

In this section, we investigate star formation in the *High-z Run* using the most massive target halo. The upper left panel of Figure 12 presents the SFR_3 of Halo 5 as a function of cosmic time, star formation rate averaged over 3 Myr to capture the rapid variability of the SFR. All participating codes exhibit fluctuations on timescales from a few to tens of Myr, showing bursty star formation. The bottom left panel shows the same SFRs averaged over 50 Myr (SFR_{50}), comparable to observationally inferred timescales. This smoothing reduces short-term burstiness and inter-code scatter, indicating that

bursty star formation features are not easily captured from observation.

The systematic differences among codes are also evident. Particle-based codes generally show higher SFRs than mesh-based codes, reflecting differences in the underlying numerical solvers. When the Jeans length becomes unresolved, particle-based codes allow gas to collapse to much higher densities, whereas mesh-based codes tend to stabilize collapse earlier by enforcing a minimum cell size (Hu et al. 2023). Also, particle-based codes are effective for shock capturing, but they could broaden contact discontinuities and smear pressure gradients, allowing cold and dense gas to remain coherent and form long-lived clumps. By contrast, mesh codes with Riemann solvers naturally resolve shocks and shear flows more sharply, leading to faster clump disruption. As a consequence, illustrated in Figure 4, particle-based codes reach gas number densities of $n_{\text{H}} \sim 3000 \text{ cm}^{-3}$, with some even exceeding 10000 cm^{-3} , potentially driving the bursty star formation characteristic of Cosmic Dawn. Even within the same hydrodynamic solver, differences emerge.

ENZO exhibits a relatively smooth rise in SFR, while RAMSES shows stronger fluctuations, likely due to its feedback prescription. RAMSES employs a delayed-cooling model, which suppresses star formation more effectively on short timescales than purely thermal injection schemes by generating a strong dense outflow (Rosdahl et al. 2017).

The growth of galaxies is mainly dominated by the mass growth of the host dark matter halo. In the right panel, we compute two star formation efficiencies, instantaneous star formation efficiency $\epsilon_{\text{inst}} = \dot{M}_*/(\dot{M}_{\text{vir}}f_b)$ and integrated star formation efficiency $\epsilon_{\text{int}} \equiv M_*/(M_{\text{vir}}f_b)$, where $f_b = 0.165$ is the baryon fraction of the universe adopted in the *High-z Run*. The definitions capture complementary aspects of the baryon-to-star conversion process. The instantaneous SFE traces the ratio of current star formation rate to the halo accretion rate, whereas the integrated SFE quantifies the cumulative efficiency of assembling the stellar mass relative to the integrated baryon inflow.

The overall behavior mirrors the SFR histories as the halo mass growth is similar across the codes. Since ϵ_{inst} responds to the instantaneous balance of gas supply and feedback, it can reach higher values and exhibit larger dispersion than ϵ_{int} . Compared with the FirstLight (Ceverino et al. 2024) simulation, the value and scatter of ϵ_{inst} in the *High-z Run* are comparable. In contrast, the scatter of ϵ_{int} is much smaller in FirstLight but remains large in the *High-z Run*. This difference reflects the single feedback model used in FirstLight, which regulates star formation across the galaxy population toward similar cumulative efficiencies, whereas the *High-z Run* compares multiple codes with distinct feedback implementations. The diversity in feedback prescriptions leads to a broader range of ϵ_{int} , indicating that star formation in the high-redshift is very sensitive to the feedback description. In our setup, we impose a fixed star formation efficiency of 1%. ENZO and CHANGA yield ϵ_{int} values consistent with this assumption, the other codes predict substantially higher efficiencies.

GIZMO reaches $\epsilon_{\text{inst}} \sim 1$ at $z = 10$, corresponding to a stellar mass of $3 \times 10^9 M_\odot$ and gas densities of $\sim 10000 \text{ cm}^{-3}$. Such extreme values resemble the predictions of Dekel et al. (2023), suggesting that feedback regulation in GIZMO is inefficient under these conditions. Indeed, Fukushima & Yajima (2021) shows that feedback can be inefficient in compact and massive clouds, resulting in a very high SFE. However, it should be emphasized that the spatial resolution of particle-based runs is $\sim 80 \text{ pc}$, which is insufficient to resolve and examine the internal structure of galaxies to verify the FFB model or other mechanism for the *High-z Run*. In the future, a more extensive analysis with a higher resolution simulation will be conducted to investigate the formation of high-redshift galaxies.

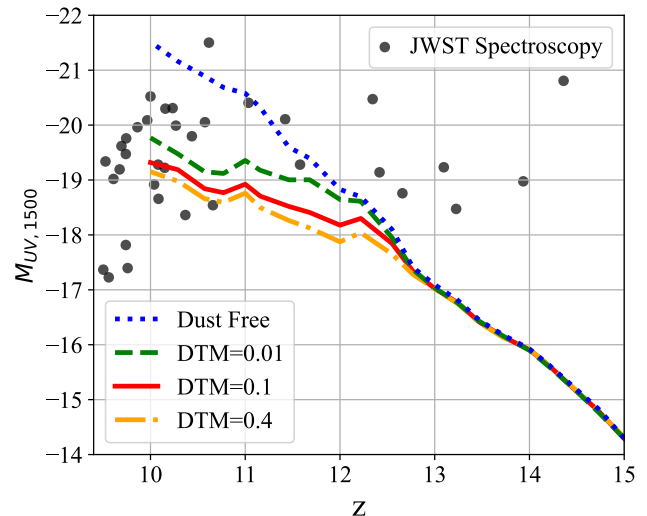


Figure 13. Same as the bottom right panel of Figure 11, but with different dust-to-metal ratios (DTM ratio= 0.01, 0.1, and 0.4) and a dust-free model. Variations in the DTM ratio produce mild differences, whereas the absence of dust decreases the UV magnitude by nearly 2 magnitudes at $z = 10$. See Section 4.2 for more information.

4.2. Effect of Dust Attenuation

Dust physics is especially uncertain above the reionization era due to the faint signal of high-redshift galaxies and limited wavelength. While recent studies (e.g., Sommovigo & Algera 2025) have attempted to constrain the dust properties of high-redshift galaxies, there are still ongoing degeneracies with dust temperature, which makes it difficult to estimate the dust mass.

To investigate this uncertainty, we vary the DTM ratio over a range of 0.01, 0.1, 0.4, and a dust-free (only consider star particles) model using SKIRT. Figure 13 illustrates the effect of dust attenuation on the average of the rest-frame UV magnitude of Halo 5 in the *High-z Run*, compared against JWST spectroscopy data. At $z > 13$, all models converge closely, indicating that dust might have only a minor effect on the brightest high-redshift galaxies similar to the ones studied here. Since the dust density is proportional to the gas density and metallicity, the dust mass in this regime is very small compared to the stellar mass due to low density and metallicity.³ However, after $z \sim 13$, the dust-free model clearly increases, producing UV magnitudes nearly two magnitudes brighter than dust-attenuated cases, while the three dusty models remain relatively close to each other.

³ RAMSES exhibits a very high metallicity due to active star formation even at $z > 13$, but at the same time, stellar feedback lowers the gas density, limiting the dust mass.

The comparison highlights that the presence of dust, rather than the precise DTM ratio, is the dominant factor in suppression of UV luminosity. Even the DTM ratio of 0.01 reduces the UV brightness significantly compared to the dust-free case, while increasing the DTM ratio to 0.4 only modestly enhances attenuation. This suggests that uncertainties in the exact efficiency of dust formation at these redshifts may be less important than whether dust is present at all. Observationally, the JWST spectroscopic points lie between the dust-free and dusty models, showing that dust extinction is already non-negligible at $z \sim 10 - 12$, although its precise abundance remains difficult to constrain. The sensitivity to dust, however, differs across codes. While varying the DTM ratio between 0.01 and 0.4 produces a small change in most cases, the contrast between dusty and dust-free models varies considerably. Due to the large reservoir of cold and dense gas in the center of particle-based codes, they also produce more dust mass, which leads to stronger attenuation than in mesh-based codes. GIZMO shows the largest differences between the DTM ratio = 0.1 model and the dust-free model at $z = 10$, RAMSES has the smallest difference. Differences of all participating codes are provided in Appendix C.

4.3. Limitations & Caveats

Despite its success in reproducing some JWST observation data, the *High- z Run* suite has several limitations.

- Our target resolution of a few tens of parsecs does not resolve the internal structure of galaxies such as giant molecular clouds, which have a scale length of the Jeans length $\lambda_J = c_s / \sqrt{G\rho/\pi}$. For gas at the threshold density for the FFB scenario ($\sim 3 \times 10^3 \text{ cm}^{-3}$) and $T \sim 300 \text{ K}$, the Jeans length falls below 10 pc and this is well beneath our resolution. Consequently, we cannot directly capture the fragmentation of dense clumps or validate small-scale star formation conditions. Instead, we can only test whether our simulation results with coarse resolution is broadly consistent with the proposed galaxy/star formation scenarios.
- Recent studies strongly suggest the presence of AGN even in galaxies at $z \sim 10$ (e.g., [Napolitano et al. 2025](#)). The *High- z Run*, however, does not include black hole seeding or AGN feedback processes. As mentioned before, AGN may not dominate the UV luminosity budget (e.g., [Ono et al. 2023](#); [Trinca et al. 2024](#)), but their mechanical and radiative feedback could have significant effects on star formation, CGM heating, and the observed spectral energy distribution (SED). A more complete model of galaxy formation at high redshift should therefore include AGN physics.

- We do not follow primordial non-equilibrium H, H₂, and He chemistry. Instead, we impose a metallicity floor of $10^{-4} Z_\odot$ to approximate early enrichment from Pop III stars. Because our target halos already reach $M_{\text{vir}} \sim 10^9 M_\odot$ by $z = 15$, cooling is expected to be dominated by atomic processes rather than molecular hydrogen ([Yoshida et al. 2003](#)), we therefore expect this choice to have little impact on the overall galaxy properties. However, primordial chemistry can be significant in low-metallicity gas at Cosmic Dawn, potentially altering the thermal balance, fragmentation, and star formation in the earliest systems.
- Finally, simulated galaxies should be compared only with observed systems whose halo masses match those of our simulated halos at the same redshift. However, because most high-redshift observational data lack any halo mass estimates, we can only suggest that the *High- z Run* galaxies fall broadly within the range of observed properties. To fully and accurately validate our results, future work will require refined semi-analytic models and dedicated survey data that probes dynamical tracers of halo masses.

5. SUMMARY AND CONCLUSION

In this paper, we presented results from the *AGORA High- z Run*, a suite of cosmological zoom-in simulations targeting massive galaxies at Cosmic Dawn ($z \geq 10$). Using six state-of-the-art hydrodynamical codes, we study inter-code agreements and differences in the high-redshift environment, and compare the simulated galaxies against JWST observation data. Our main findings are summarized as follows:

- Despite differences in feedback implementations among the simulation codes, the stellar mass histories exhibit a broad convergence across codes (Figure 5). In contrast, the metallicity evolution shows substantial inter-code variation, reflecting the diversity in feedback prescriptions (Figure 8). The mass–metallicity relation displays a remarkably tight positive correlation in most codes (Figure 9), demonstrating the overall robustness of galaxy formation models irrespective of the specific numerical schemes adopted.
- Without additional subgrid physics, the *High- z Run* galaxies in massive halos succeed in reproducing galactic properties (Figures 5, 8 and 11) that are comparable to JWST observation data at $z \leq 12$. Although the *High- z Run* galaxies underpredict galaxy properties $z \sim 13 - 14$, these results suggest that “vanilla” Λ CDM galaxy formation framework can sufficiently

account for galaxies at Cosmic Dawn if the host halo is massive enough.

- Some galaxies in the *High-z Run* exhibit the signatures that are broadly consistent with the feedback-free starburst model ($n_{\text{H}} > 3000 \text{ cm}^{-3}$, $\text{SFR} \sim 60 M_{\odot}/\text{yr}$, $\epsilon_{\text{inst}} > 0.2$; Figures 4 and 12). Although we impose a fixed local star formation efficiency of 1% in all our simulations, these galaxies show significantly higher SFE, reflecting the rapid conversion of gas into stars in dense environments. However, we cannot readily verify this scenario since the resolution of the *High-z Run* is not sufficient to resolve internal galactic structure.
- The presence of dust plays a crucial role in determining the UV luminosities of the simulated galaxies in the *High-z Run*. At $z > 13$, the difference between dust-free and dust-included models remains minimal, suggesting that dust has little impact on the earliest galaxies. However, at later times, the dust-free model predicts UV luminosities up to ~ 2 magnitudes brighter than the dust-included cases, highlighting the strong attenuation effect once dust exists. In contrast, variations in the dust-to-metal ratio introduce only a minor difference, indicating that the key factor is the presence of dust itself rather than its precise abundance (Figure 13).

The *AGORA High-z Run* is the first step toward understanding the formation and evolution of galaxies at Cosmic Dawn, as well as the effect of different gravity and hydrodynamics schemes in the high-redshift environment. Despite its limitations such as insufficient resolution and simplified subgrid physics, this suite of simulations offers valuable insights that pave the way for more refined, computationally

expensive future simulations. Indeed, we plan to carry out the new “*High-res High-z Run*” suite with higher spatial resolution (effective resolution of $\leq 10 \text{ pc}$) and sophisticated physical processes, enabling a more realistic exploration of galaxy formation in the early universe.

J.-H.K.’s work was supported by the National Research Foundation of Korea (NRF) grant funded by the Korea government (MSIT) (No. 2022M3K3A1093827 and No. 2023R1A2C1003244). His work was also supported by the National Institute of Supercomputing and Network/Korea Institute of Science and Technology Information with supercomputing resources including technical support, grants KSC-2021-CRE-0442, KSC-2022-CRE-0355 and KSC-2024-CRE-0232. His work was also supported by the GlobalLAMP Program of the NRF grant funded by the Ministry of Education (No. RS-2023-00301976). D.C. is supported by research grant PID2021-122603NB-C21 funded by the Ministerio de Ciencia, Innovación y Universidades (MI-CIU/FEDER) and the research grant CNS2024-154550 funded by MI-CIU/AEI/10.13039/501100011033. GADGET-4 simulations were performed using the SQUID at the D3 Center, the University of Osaka, through the HPCI System Research Project (hp230089, hp240141, hp250119). KN is partly supported by the MEXT/JSPS KAKENHI Grant Numbers JP20H00180, JP22K21349, 24H00002, 24H00241 and 25K01032 (K.N.). HV was supported by DGAPA-PAPIIT-UNAM project IN111425. CHANGA runs were carried out in the CNS-IPICYT-SECIHTI, LNS-SECIHTI, and LAMOD-UNAM. R.R.C. acknowledges financial support from the Spanish Ministry of Science and Innovation through the research grant PID2021-123417OB-I00, funded by MCIN/AEI/10.13039/501100011033/FEDER, EU. and from IND2022/TIC-23643 project funded by Comunidad de Madrid.

REFERENCES

- Adams, N. J., Conselice, C. J., Ferreira, L., et al. 2023, *MNRAS*, 518, 4755, doi: [10.1093/mnras/stac3347](https://doi.org/10.1093/mnras/stac3347)
- Andalman, Z. L., Teyssier, R., & Dekel, A. 2025, *MNRAS*, 540, 3350, doi: [10.1093/mnras/staf930](https://doi.org/10.1093/mnras/staf930)
- Aoyama, S., Hou, K.-C., Shimizu, I., et al. 2017, *MNRAS*, 466, 105, doi: [10.1093/mnras/stw3061](https://doi.org/10.1093/mnras/stw3061)
- Arrabal Haro, P., Dickinson, M., Finkelstein, S. L., et al. 2023, *Nature*, 622, 707, doi: [10.1038/s41586-023-06521-7](https://doi.org/10.1038/s41586-023-06521-7)
- Behrens, C., Pallottini, A., Ferrara, A., Gallerani, S., & Vallini, L. 2018, *MNRAS*, 477, 552, doi: [10.1093/mnras/sty552](https://doi.org/10.1093/mnras/sty552)
- Behroozi, P., Conroy, C., Wechsler, R. H., et al. 2020, *MNRAS*, 499, 5702, doi: [10.1093/mnras/staa3164](https://doi.org/10.1093/mnras/staa3164)
- Behroozi, P. S., Wechsler, R. H., & Wu, H.-Y. 2013, *ApJ*, 762, 109, doi: [10.1088/0004-637X/762/2/109](https://doi.org/10.1088/0004-637X/762/2/109)
- Bhatawdekar, R., Conselice, C. J., Margalef-Bentabol, B., & Duncan, K. 2019, *MNRAS*, 486, 3805, doi: [10.1093/mnras/stz866](https://doi.org/10.1093/mnras/stz866)
- Bouwens, R. J., Stefanon, M., Brammer, G., et al. 2023, *MNRAS*, 523, 1036, doi: [10.1093/mnras/stad1145](https://doi.org/10.1093/mnras/stad1145)
- Boylan-Kolchin, M. 2023, *Nature Astronomy*, 7, 731, doi: [10.1038/s41550-023-01937-7](https://doi.org/10.1038/s41550-023-01937-7)
- Bryan, G. L., Norman, M. L., O’Shea, B. W., et al. 2014, *ApJS*, 211, 19, doi: [10.1088/0067-0049/211/2/19](https://doi.org/10.1088/0067-0049/211/2/19)

- Bunker, A. J., Saxena, A., Cameron, A. J., et al. 2023, *A&A*, 677, A88, doi: [10.1051/0004-6361/202346159](https://doi.org/10.1051/0004-6361/202346159)
- Camps, P., & Baes, M. 2020, *Astronomy and Computing*, 31, 100381, doi: [10.1016/j.ascom.2020.100381](https://doi.org/10.1016/j.ascom.2020.100381)
- Carniani, S., Hainline, K., D'Eugenio, F., et al. 2024, *Nature*, 633, 318, doi: [10.1038/s41586-024-07860-9](https://doi.org/10.1038/s41586-024-07860-9)
- Carniani, S., D'Eugenio, F., Ji, X., et al. 2025, *A&A*, 696, A87, doi: [10.1051/0004-6361/202452451](https://doi.org/10.1051/0004-6361/202452451)
- Castellano, M., Fontana, A., Treu, T., et al. 2022, *ApJL*, 938, L15, doi: [10.3847/2041-8213/ac94d0](https://doi.org/10.3847/2041-8213/ac94d0)
- Castellano, M., Napolitano, L., Fontana, A., et al. 2024, *ApJ*, 972, 143, doi: [10.3847/1538-4357/ad5f88](https://doi.org/10.3847/1538-4357/ad5f88)
- Castellano, M., Fontana, A., Merlin, E., et al. 2025, arXiv e-prints, arXiv:2504.05893, doi: [10.48550/arXiv.2504.05893](https://doi.org/10.48550/arXiv.2504.05893)
- Ceverino, D., Klessen, R. S., & Glover, S. C. O. 2019, *MNRAS*, 484, 1366, doi: [10.1093/mnras/stz079](https://doi.org/10.1093/mnras/stz079)
- Ceverino, D., Nakazato, Y., Yoshida, N., Klessen, R. S., & Glover, S. C. O. 2024, *A&A*, 689, A244, doi: [10.1051/0004-6361/202450224](https://doi.org/10.1051/0004-6361/202450224)
- Chabrier, G. 2003, *PASP*, 115, 763, doi: [10.1086/376392](https://doi.org/10.1086/376392)
- Chon, S., Ono, H., Omukai, K., & Schneider, R. 2022, *MNRAS*, 514, 4639, doi: [10.1093/mnras/stac1549](https://doi.org/10.1093/mnras/stac1549)
- Curtis-Lake, E., Carniani, S., Cameron, A., et al. 2023, *Nature Astronomy*, 7, 622, doi: [10.1038/s41550-023-01918-w](https://doi.org/10.1038/s41550-023-01918-w)
- De Vis, P., Jones, A., Viaene, S., et al. 2019, *A&A*, 623, A5, doi: [10.1051/0004-6361/201834444](https://doi.org/10.1051/0004-6361/201834444)
- Dekel, A., & Birnboim, Y. 2006, *MNRAS*, 368, 2, doi: [10.1111/j.1365-2966.2006.10145.x](https://doi.org/10.1111/j.1365-2966.2006.10145.x)
- Dekel, A., Sarkar, K. C., Birnboim, Y., Mandelker, N., & Li, Z. 2023, *MNRAS*, 523, 3201, doi: [10.1093/mnras/stad1557](https://doi.org/10.1093/mnras/stad1557)
- Donnan, C. T., McLeod, D. J., Dunlop, J. S., et al. 2023, *MNRAS*, 518, 6011, doi: [10.1093/mnras/stac3472](https://doi.org/10.1093/mnras/stac3472)
- Dubois, Y., Volonteri, M., Silk, J., et al. 2015, *MNRAS*, 452, 1502, doi: [10.1093/mnras/stv1416](https://doi.org/10.1093/mnras/stv1416)
- Ellis, R. S., McLure, R. J., Dunlop, J. S., et al. 2013, *ApJL*, 763, L7, doi: [10.1088/2041-8205/763/1/L7](https://doi.org/10.1088/2041-8205/763/1/L7)
- Feldmann, R., Boylan-Kolchin, M., Bullock, J. S., et al. 2025, *MNRAS*, 536, 988, doi: [10.1093/mnras/stae2633](https://doi.org/10.1093/mnras/stae2633)
- Ferland, G. J., Porter, R. L., van Hoof, P. A. M., et al. 2013, *RMxAA*, 49, 137, doi: [10.48550/arXiv.1302.4485](https://doi.org/10.48550/arXiv.1302.4485)
- Ferrara, A., Pallottini, A., & Sommovigo, L. 2025, *A&A*, 694, A286, doi: [10.1051/0004-6361/202452707](https://doi.org/10.1051/0004-6361/202452707)
- Finkelstein, S. L., Bagley, M., Song, M., et al. 2022, *ApJ*, 928, 52, doi: [10.3847/1538-4357/ac3aed](https://doi.org/10.3847/1538-4357/ac3aed)
- Finkelstein, S. L., Bagley, M. B., Ferguson, H. C., et al. 2023, *ApJL*, 946, L13, doi: [10.3847/2041-8213/acade4](https://doi.org/10.3847/2041-8213/acade4)
- Finkelstein, S. L., Leung, G. C. K., Bagley, M. B., et al. 2024, *ApJL*, 969, L2, doi: [10.3847/2041-8213/ad4495](https://doi.org/10.3847/2041-8213/ad4495)
- Fukushima, H., & Yajima, H. 2021, *MNRAS*, 506, 5512, doi: [10.1093/mnras/stab2099](https://doi.org/10.1093/mnras/stab2099)
- Gunn, J. E., & Peterson, B. A. 1965, *ApJ*, 142, 1633, doi: [10.1086/148444](https://doi.org/10.1086/148444)
- Haardt, F., & Madau, P. 2012, *ApJ*, 746, 125, doi: [10.1088/0004-637X/746/2/125](https://doi.org/10.1088/0004-637X/746/2/125)
- Hahn, O., & Abel, T. 2011, *MNRAS*, 415, 2101, doi: [10.1111/j.1365-2966.2011.18820.x](https://doi.org/10.1111/j.1365-2966.2011.18820.x)
- Harikane, Y., Nakajima, K., Ouchi, M., et al. 2024, *ApJ*, 960, 56, doi: [10.3847/1538-4357/ad0b7e](https://doi.org/10.3847/1538-4357/ad0b7e)
- Harikane, Y., Inoue, A. K., Ellis, R. S., et al. 2025, *ApJ*, 980, 138, doi: [10.3847/1538-4357/ad9b2c](https://doi.org/10.3847/1538-4357/ad9b2c)
- Hayward, C. C., & Hopkins, P. F. 2017, *MNRAS*, 465, 1682, doi: [10.1093/mnras/stw2888](https://doi.org/10.1093/mnras/stw2888)
- Heintz, K. E., De Cia, A., Thöne, C. C., et al. 2023, *A&A*, 679, A91, doi: [10.1051/0004-6361/202347418](https://doi.org/10.1051/0004-6361/202347418)
- Hopkins, P. F. 2015, *MNRAS*, 450, 53, doi: [10.1093/mnras/stv195](https://doi.org/10.1093/mnras/stv195)
- Hopkins, P. F., Wetzel, A., Kereš, D., et al. 2018, *MNRAS*, 477, 1578, doi: [10.1093/mnras/sty674](https://doi.org/10.1093/mnras/sty674)
- Hsiao, T. Y.-Y., Abdurro'uf, Coe, D., et al. 2024, *ApJ*, 973, 8, doi: [10.3847/1538-4357/ad5da8](https://doi.org/10.3847/1538-4357/ad5da8)
- Hu, C.-Y., Smith, M. C., Teyssier, R., et al. 2023, *ApJ*, 950, 132, doi: [10.3847/1538-4357/accf9e](https://doi.org/10.3847/1538-4357/accf9e)
- Inayoshi, K., Harikane, Y., Inoue, A. K., Li, W., & Ho, L. C. 2022, *ApJL*, 938, L10, doi: [10.3847/2041-8213/ac9310](https://doi.org/10.3847/2041-8213/ac9310)
- Jeong, T. B., Jeon, M., Song, H., & Bromm, V. 2025, *ApJ*, 980, 10, doi: [10.3847/1538-4357/ada27d](https://doi.org/10.3847/1538-4357/ada27d)
- Jung, M., Roca-Fàbrega, S., Kim, J.-H., et al. 2024, *ApJ*, 964, 123, doi: [10.3847/1538-4357/ad245b](https://doi.org/10.3847/1538-4357/ad245b)
- Jung, M., Kim, J.-h., Nguyen, T. H., et al. 2025, arXiv e-prints, arXiv:2505.05720, doi: [10.48550/arXiv.2505.05720](https://doi.org/10.48550/arXiv.2505.05720)
- Kang, C., Kimm, T., Han, D., et al. 2025, *A&A*, 693, A149, doi: [10.1051/0004-6361/202451502](https://doi.org/10.1051/0004-6361/202451502)
- Kannan, R., Puchwein, E., Smith, A., et al. 2025, *The Open Journal of Astrophysics*, 8, 153, doi: [10.33232/001c.145804](https://doi.org/10.33232/001c.145804)
- Kapoor, A. U., Baes, M., van der Wel, A., et al. 2023, *MNRAS*, 526, 3871, doi: [10.1093/mnras/stad2977](https://doi.org/10.1093/mnras/stad2977)
- Keller, B. W., Wadsley, J., Benincasa, S. M., & Couchman, H. M. P. 2014, *MNRAS*, 442, 3013, doi: [10.1093/mnras/stu1058](https://doi.org/10.1093/mnras/stu1058)
- Kim, J.-h., Abel, T., Agertz, O., et al. 2014, *ApJS*, 210, 14, doi: [10.1088/0067-0049/210/1/14](https://doi.org/10.1088/0067-0049/210/1/14)
- Kim, J.-h., Agertz, O., Teyssier, R., et al. 2016, *ApJ*, 833, 202, doi: [10.3847/1538-4357/833/2/202](https://doi.org/10.3847/1538-4357/833/2/202)
- Konstantopoulou, C., De Cia, A., Ledoux, C., et al. 2024, *A&A*, 681, A64, doi: [10.1051/0004-6361/202347171](https://doi.org/10.1051/0004-6361/202347171)
- Labbé, I., van Dokkum, P., Nelson, E., et al. 2023, *Nature*, 616, 266, doi: [10.1038/s41586-023-05786-2](https://doi.org/10.1038/s41586-023-05786-2)
- Langan, I., Ceverino, D., & Finlator, K. 2020, *MNRAS*, 494, 1988, doi: [10.1093/mnras/staa880](https://doi.org/10.1093/mnras/staa880)
- Leung, G. C. K., Bagley, M. B., Finkelstein, S. L., et al. 2023, *ApJL*, 954, L46, doi: [10.3847/2041-8213/acf365](https://doi.org/10.3847/2041-8213/acf365)

- Li, Z., Dekel, A., Sarkar, K. C., et al. 2024, *A&A*, 690, A108, doi: [10.1051/0004-6361/202348727](https://doi.org/10.1051/0004-6361/202348727)
- Lovell, C. C., Harrison, I., Harikane, Y., Tacchella, S., & Wilkins, S. M. 2023, *MNRAS*, 518, 2511, doi: [10.1093/mnras/stac3224](https://doi.org/10.1093/mnras/stac3224)
- Mainali, R., Zitrin, A., Stark, D. P., et al. 2018, *MNRAS*, 479, 1180, doi: [10.1093/mnras/sty1640](https://doi.org/10.1093/mnras/sty1640)
- Marszewski, A., Sun, G., Faucher-Giguère, C.-A., Hayward, C. C., & Feldmann, R. 2024, *ApJL*, 967, L41, doi: [10.3847/2041-8213/ad4cee](https://doi.org/10.3847/2041-8213/ad4cee)
- McCaffrey, J., Hardin, S., Wise, J. H., & Regan, J. A. 2023, *The Open Journal of Astrophysics*, 6, 47, doi: [10.21105/astro.2304.13755](https://doi.org/10.21105/astro.2304.13755)
- Menon, H., Wesolowski, L., Zheng, G., et al. 2015, *Computational Astrophysics and Cosmology*, 2, 1, doi: [10.1186/s40668-015-0007-9](https://doi.org/10.1186/s40668-015-0007-9)
- Moster, B. P., Somerville, R. S., Maulbetsch, C., et al. 2010, *ApJ*, 710, 903, doi: [10.1088/0004-637X/710/2/903](https://doi.org/10.1088/0004-637X/710/2/903)
- Napolitano, L., Castellano, M., Pentericci, L., et al. 2025, *A&A*, 693, A50, doi: [10.1051/0004-6361/202452090](https://doi.org/10.1051/0004-6361/202452090)
- Oesch, P. A., Brammer, G., van Dokkum, P. G., et al. 2016, *ApJ*, 819, 129, doi: [10.3847/0004-637X/819/2/129](https://doi.org/10.3847/0004-637X/819/2/129)
- Oke, J. B., & Gunn, J. E. 1983, *ApJ*, 266, 713, doi: [10.1086/160817](https://doi.org/10.1086/160817)
- Oku, Y., & Nagamine, K. 2024, *ApJ*, 975, 183, doi: [10.3847/1538-4357/ad77d3](https://doi.org/10.3847/1538-4357/ad77d3)
- Oku, Y., Tomida, K., Nagamine, K., Shimizu, I., & Cen, R. 2022, *ApJS*, 262, 9, doi: [10.3847/1538-4365/ac77ff](https://doi.org/10.3847/1538-4365/ac77ff)
- Ono, Y., Harikane, Y., Ouchi, M., et al. 2023, *ApJ*, 951, 72, doi: [10.3847/1538-4357/acd44a](https://doi.org/10.3847/1538-4357/acd44a)
- Pérez-González, P. G., Östlin, G., Costantin, L., et al. 2025, *ApJ*, 991, 179, doi: [10.3847/1538-4357/adf8c9](https://doi.org/10.3847/1538-4357/adf8c9)
- Revaz, Y., & Jablonka, P. 2012, *A&A*, 538, A82, doi: [10.1051/0004-6361/201117402](https://doi.org/10.1051/0004-6361/201117402)
- Robertson, B., Johnson, B. D., Tacchella, S., et al. 2024, *ApJ*, 970, 31, doi: [10.3847/1538-4357/ad463d](https://doi.org/10.3847/1538-4357/ad463d)
- Robertson, B. E., Tacchella, S., Johnson, B. D., et al. 2023, *Nature Astronomy*, 7, 611, doi: [10.1038/s41550-023-01921-1](https://doi.org/10.1038/s41550-023-01921-1)
- Roca-Fàbrega, S., Kim, J.-H., Hausammann, L., et al. 2021, *ApJ*, 917, 64, doi: [10.3847/1538-4357/ac088a](https://doi.org/10.3847/1538-4357/ac088a)
- Roca-Fàbrega, S., Kim, J.-H., Primack, J. R., et al. 2024, *ApJ*, 968, 125, doi: [10.3847/1538-4357/ad43de](https://doi.org/10.3847/1538-4357/ad43de)
- Rodríguez-Cardoso, R., Roca-Fàbrega, S., Jung, M., et al. 2025, *A&A*, 698, A303, doi: [10.1051/0004-6361/202453639](https://doi.org/10.1051/0004-6361/202453639)
- Rosdahl, J., Schaye, J., Dubois, Y., Kimm, T., & Teyssier, R. 2017, *MNRAS*, 466, 11, doi: [10.1093/mnras/stw3034](https://doi.org/10.1093/mnras/stw3034)
- Saitoh, T. R. 2017, *AJ*, 153, 85, doi: [10.3847/1538-3881/153/2/85](https://doi.org/10.3847/1538-3881/153/2/85)
- Schouws, S., Bouwens, R. J., Ormerod, K., et al. 2025, *ApJ*, 988, 19, doi: [10.3847/1538-4357/adbf1b](https://doi.org/10.3847/1538-4357/adbf1b)
- Shimizu, I., Todoroki, K., Yajima, H., & Nagamine, K. 2019, *MNRAS*, 484, 2632, doi: [10.1093/mnras/stz098](https://doi.org/10.1093/mnras/stz098)
- Smith, B. D., Bryan, G. L., Glover, S. C. O., et al. 2017, *MNRAS*, 466, 2217, doi: [10.1093/mnras/stw3291](https://doi.org/10.1093/mnras/stw3291)
- Sommovigo, L., & Algera, H. 2025, *MNRAS*, 540, 3693, doi: [10.1093/mnras/staf897](https://doi.org/10.1093/mnras/staf897)
- Springel, V. 2005, *MNRAS*, 364, 1105, doi: [10.1111/j.1365-2966.2005.09655.x](https://doi.org/10.1111/j.1365-2966.2005.09655.x)
- . 2010, *MNRAS*, 401, 791, doi: [10.1111/j.1365-2966.2009.15715.x](https://doi.org/10.1111/j.1365-2966.2009.15715.x)
- Springel, V., Pakmor, R., Zier, O., & Reinecke, M. 2021, *MNRAS*, 506, 2871, doi: [10.1093/mnras/stab1855](https://doi.org/10.1093/mnras/stab1855)
- Stanway, E. R., & Eldridge, J. J. 2018, *MNRAS*, 479, 75, doi: [10.1093/mnras/sty1353](https://doi.org/10.1093/mnras/sty1353)
- Strawn, C., Roca-Fàbrega, S., Primack, J. R., et al. 2024, *ApJ*, 962, 29, doi: [10.3847/1538-4357/ad12cb](https://doi.org/10.3847/1538-4357/ad12cb)
- Sun, G., Faucher-Giguère, C.-A., Hayward, C. C., & Shen, X. 2023, *MNRAS*, 526, 2665, doi: [10.1093/mnras/stad2902](https://doi.org/10.1093/mnras/stad2902)
- Tacchella, S., Eisenstein, D. J., Hainline, K., et al. 2023, *ApJ*, 952, 74, doi: [10.3847/1538-4357/acdbcb](https://doi.org/10.3847/1538-4357/acdbcb)
- Teyssier, R. 2002, *A&A*, 385, 337, doi: [10.1051/0004-6361:20011817](https://doi.org/10.1051/0004-6361:20011817)
- Tremonti, C. A., Heckman, T. M., Kauffmann, G., et al. 2004, *ApJ*, 613, 898, doi: [10.1086/423264](https://doi.org/10.1086/423264)
- Trinca, A., Schneider, R., Valiante, R., et al. 2024, *MNRAS*, 529, 3563, doi: [10.1093/mnras/stae651](https://doi.org/10.1093/mnras/stae651)
- Tsuna, D., Nakazato, Y., & Hartwig, T. 2023, *MNRAS*, 526, 4801, doi: [10.1093/mnras/stad3043](https://doi.org/10.1093/mnras/stad3043)
- van Dokkum, F., Capelo, P. R., Mayer, L., Reed, D. S., & Quinn, T. R. 2025, *MNRAS*, 543, 2760, doi: [10.1093/mnras/staf1638](https://doi.org/10.1093/mnras/staf1638)
- Wadsley, J. W., Keller, B. W., & Quinn, T. R. 2017, *MNRAS*, 471, 2357, doi: [10.1093/mnras/stx1643](https://doi.org/10.1093/mnras/stx1643)
- Wang, B., Fujimoto, S., Labbé, I., et al. 2023, *ApJL*, 957, L34, doi: [10.3847/2041-8213/acfe07](https://doi.org/10.3847/2041-8213/acfe07)
- Whitler, L., Stark, D. P., Topping, M. W., et al. 2025, *ApJ*, 992, 63, doi: [10.3847/1538-4357/adfdcc](https://doi.org/10.3847/1538-4357/adfdcc)
- Wilkins, S. M., Vijayan, A. P., Lovell, C. C., et al. 2023, *MNRAS*, 519, 3118, doi: [10.1093/mnras/stac3280](https://doi.org/10.1093/mnras/stac3280)
- Wu, Z., Eisenstein, D. J., Johnson, B. D., et al. 2025, *ApJ*, 992, 212, doi: [10.3847/1538-4357/ae01a1](https://doi.org/10.3847/1538-4357/ae01a1)
- Yoshida, N., Abel, T., Hernquist, L., & Sugiyama, N. 2003, *ApJ*, 592, 645, doi: [10.1086/375810](https://doi.org/10.1086/375810)
- Yung, L. Y. A., Somerville, R. S., Finkelstein, S. L., Wilkins, S. M., & Gardner, J. P. 2024, *MNRAS*, 527, 5929, doi: [10.1093/mnras/stad3484](https://doi.org/10.1093/mnras/stad3484)
- Yung, L. Y. A., Somerville, R. S., Popping, G., et al. 2019, *MNRAS*, 490, 2855, doi: [10.1093/mnras/stz2755](https://doi.org/10.1093/mnras/stz2755)

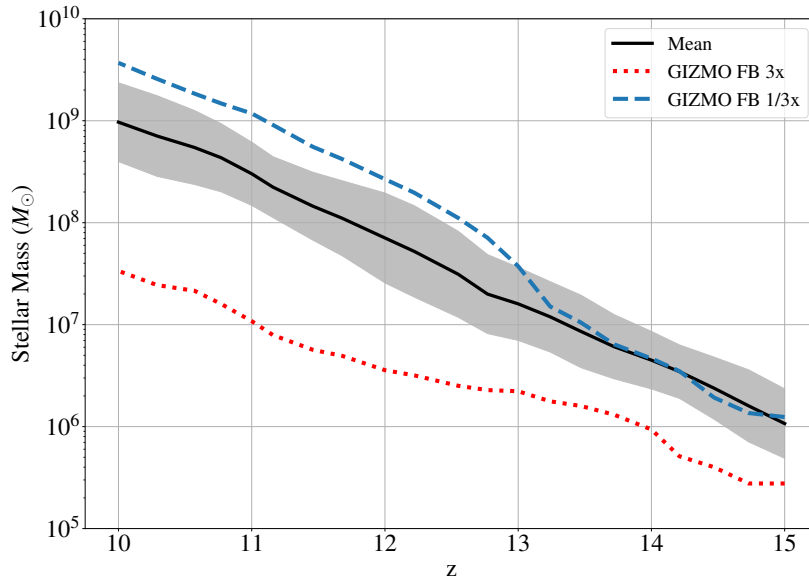


Figure 14. Same as Figure 5, but mean stellar mass evolution for Halo 4, with the black line indicating the average of participating codes and the gray shaded region representing the 1σ scatter. The colored lines show the results from additional feedback convergence tests using GIZMO — red dotted line and blue dashed line correspond to GIZMO simulations with 3 times stronger and weaker supernova feedback energy, respectively. See Appendix A for more information.

APPENDIX

A. INTER-CODE CONVERGENCE TEST IN THE STELLAR MASS

Figure 14 shows the same stellar mass history of Halo 4 from Figure 5, but with the additional convergence test results. The black line indicates the mean stellar mass across all codes, and the shaded region represents the one standard deviation of participating codes. The red dotted line and blue dashed line indicate the evolution of stellar mass using GIZMO with feedback strength varied by a factor of 3. Each test line differs from the original simulation by nearly an order of magnitude. Although the difference between the minimum and maximum values among codes can reach 1 dex, the inter-code results generally show better convergence than the feedback variation lines, especially considering the substantial diversity in feedback implementations across the codes.

B. MOCK IMAGES WITH DIFFERENT RESOLUTIONS AND RGB BANDS

In Figure 15, we compare mock images generated from SKIRT at two different resolutions. We also apply different RGB composite filters (R: F1000W, G: F444W, B: F277W) to examine the effects of dust on the mock images. The upper row corresponds to the JWST NIRCcam resolution, with a pixel width of $0.031''$. The bottom row, reproduced from Figure 10, has 8 times higher spatial resolution. Although the higher-resolution images appear more compact and show finer structures, the average difference in the resulting SEDs is less than 2 percent, indicating that the resolution effect on integrated photometric properties is minimal. The impact of dust, which appears as dark lanes in Figure 10, is also shown more distinctly here as brownish lanes, making the attenuation features more evident.

C. FLUX DIFFERENCES BETWEEN DIFFERENT DTM RATIOS

Figure 16 shows the SED of simulated galaxies with varying dust-to-metal ratios (DTM ratio = 0.01, 0.1, and 0.4) and a dust-free model.⁴ The upper panel demonstrates that the presence of dust substantially suppresses the UV continuum, with GIZMO exhibiting the strongest attenuation and RAMSES the weakest. Variations in the DTM ratio produce only modest deviations from

⁴ SKIRT nebular emission library assumes a shell around star-forming regions, which produces emission lines even in the dust-free model. However, the differences are also observed in the non-nebular emission library.

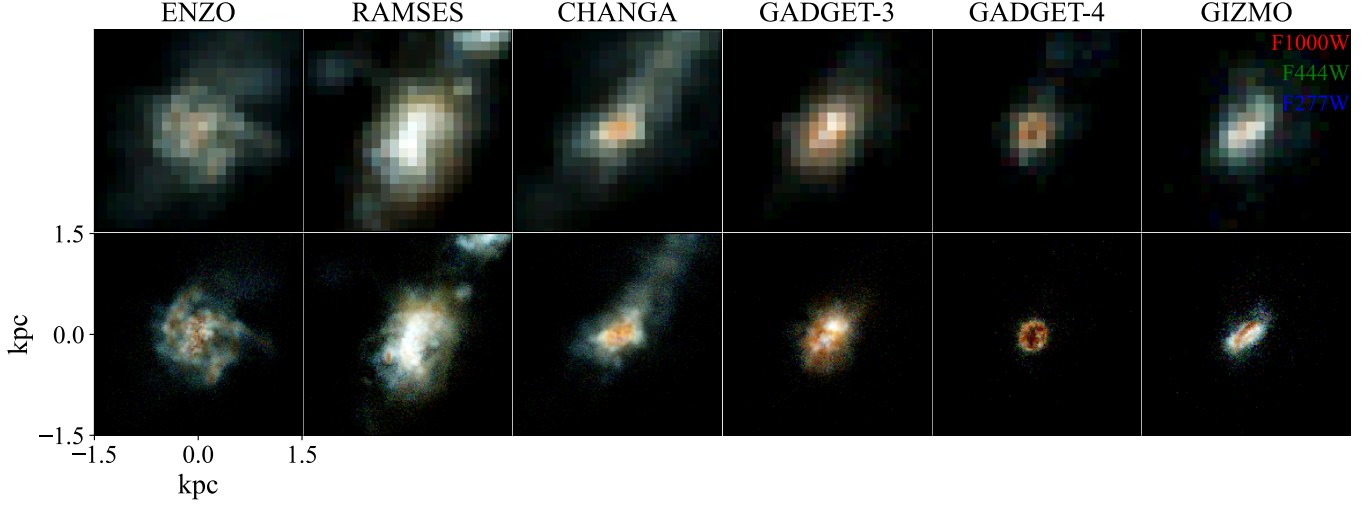


Figure 15. Comparison of mock images of a simulated galaxy at different resolutions and with different RGB composite filters (R: F1000W, G: F444W, B: F277W). The original mock image in the *bottom row* ($W_{\text{pixel}} = 0.0039''$, equivalent to 17 pc at $z = 10$) is degraded to match the resolution of JWST NIRCам in the *top row* ($W_{\text{pixel}} = 0.031''$, equivalent to 132 pc). See Appendix B for more information.

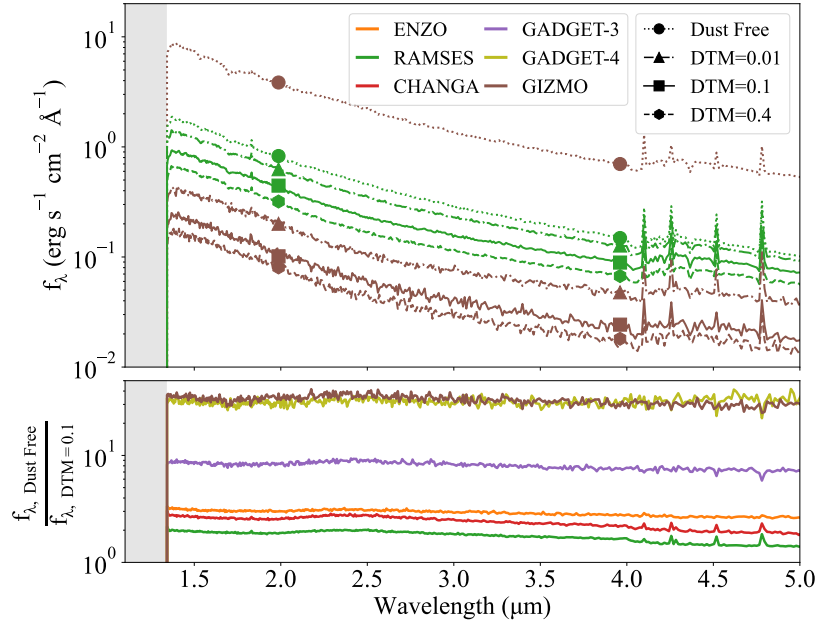


Figure 16. *Upper panel:* The simulated galaxies' spectral energy distributions (SEDs) with different dust-to-metal ratios (DTM ratio = 0.01, 0.1, and 0.4) and a dust-free model. Only two representative codes are shown here to illustrate the largest (GIZMO) and smallest (RAMSES) deviations. *Bottom panel:* The ratios of the dust-free model to the fiducial case (DTM ratio = 0.1) for all codes. See Appendix C for more information.

the fiducial model (DTM ratio = 0.1). The bottom panel presents the flux ratios of the dust-free model relative to the fiducial case, showing that dust attenuation can reduce the UV flux by factors ranging from about 2 to 30, depending on the simulation code.